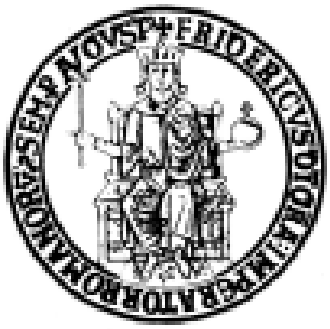

**Università degli Studi di Napoli**

**FEDERICO II**

**PhD Thesis in**

# Novel Technologies for materials sensors and imaging

# Design and characterisation of photonic quasicrystals from microwave to optical regime

**XXIII cycle**

**Coordinator: Pr. A.Andreone**

———————————————————————————————

**Defended by**

**Priya Rose T.**

# Overview

Photonic band-gap materials are artificially periodic engineered materials with which we can control and manipulate the electromagnetic radiation. The period photonic crystals are well known and have been studied for the last two decades. Recently Photonic structures lacking long-range translational order but with orientational order and higher-order rotational symmetries which are not compatible with the spatial periodicity, called "photonic quasi-crystals"(PQCs) in analogy with solid-state physics, are gaining a growing attention in view of their unique characteristics. This PhD work is devoted to the design and fabrication of photonic quasicrystals working in microwave and optical frequencies.

The first chapter of the thesis is aimed to give a general introduction to quasicrystal structures, their basic characteristics and properties. It provides a very general description of methods developed to generate quasicrystal geometries which can be useful in photonic applications. Then some of the photonic applications are explained. The last section of the chapter gives a broad idea about the fabrication methods used for photonic quasicrystals.

In the second chapter, the basic theoretical aspects on the band gap formation in photonic crystals and quasicrystals are discussed. It also describes few common computational methods used in the numerical studies of photonic structures. The Finite Difference Time domain (FDTD) is explained in detail. The final part of the chapter is devoted to analyze the results obtained by FDTD simulations in some of the selected quasicrystals. The photonic band gap formation in quasicrystal geometries with 8-, 10- and 12-fold symmetries are numerically studied and compared.

Microwave experiments carried out to study the band gap formation in low-index contrast aperiodically ordered structures are described in chapter 3. First the microwave measurement techniques used are introduced. It also gives a brief description of the instruments used in the measurements. Then the experimental results obtained for quasicrystals structures with 8-, 10- and 12-fold symmetries are reported and compared with the results from a regular

hexagonal photonic crystal structure. The study of thes isotropy preparation of the PQC band gap is also reported.

Chapter 4 is entirely devoted to describe the versatile technique of Computer Generated Holography combined with Spatial Light Modulation (SLM-CGN) that is used to fabricate the photonic structures working in the optical regime. Various aspects of the technique are explained in details. The final part of the chapter contain some of the interesting results experimentally obtained using this technique.

*Acknowledgements.....*

*I would like to thank all those who helped me to successfully complete this PhD. I wish to express my heartfelt gratitude to my advisors* ***Prof. Giancarlo Abbate*** *and* ***Prof. Antonello Andreone*** *for their valuable advices and patience. I thankfully remember all the fruitful discussion we had during the course of the PhD.*

*I thank* ***Dr. Emiliano Di Gennaro*** *and* ***Dr. Gianluigi Zito*** *for their support and help. Thanks to* ***Dr. Antigone Marino*** *for all the help she has done for me from the beginning of my stay in Napoli.*

*I have no words to express my heartfelt gratitude to* ***Mr. Guido Celentano*** *who was always had been there to help and support me.*

*Thanks to all my friends in Napoli, especially to Nassim, Dallel , Wan Khartini and Fatema for their never ending patience and support.*

*I thank my parents for always encouraging me.*

# Figures List

# Chapter 1

# Introduction to quasicrystals



# Chapter 2

# Background theory and FDTD simulations

# *Chapter 3*

# *Experiments in Microwave frequencies*

# Chapter 1

# Introduction to quasicrystals

The advances in photonics especially in the last decade makes it necessary to have suitable ways for generating and managing electromagnetic energy for various applications such as optical communication. It is important to engineer the properties of the materials which can respond to light waves of the desired frequency to confine, filter or guide the electromagnetic radiation. When it comes to question of controlling the light propagation, the answer is photonic crystals. They are analogous to the electronic crystals where instead of atoms or molecules there are low-loss dielectric materials of differing dielectric constant. The periodic dielectric function replaces the periodic potential in this case. Yablonovitch [1] showed that if the dielectric constants of the two materials are sufficiently different, the photonic crystals can also possess a photonic band-gap (PBG), so that a certain range of frequencies are not passed through the crystal, just like an electronic semi-conductor. Photonic crystals can be one-, two- or three dimensional depending on the properties of the dielectric function. A stack of alternating layers of two different dielectric materials (a Bragg mirror), represents a one-dimensional photonic crystal. The position and width of the photonics band-gap plays an important role in case of most of the applications of photonic crystals (PCs).

When the frequency of the electromagnetic radiation falls within the photonic band-gap frequencies, a photonic crystal acts like a perfect "optical insulator" for the radiation. This property can be exploited to design and build ultra-compact mirrors, cavities and waveguides [2-3]. For other frequencies which fall in a photonic band, the photonic crystal acts like an "optical conductor" which finds applications in wavelength division multiplexing [4] and beam steering. Another interesting

property of PCs is the super prism effect which relates to the propagation of radiation through the photonic crystal [5] which then also revealed negative-index refraction in PCs.

An important application of photonic crystals is in the localization of electromagnetic field. This is usually done by intentionally introducing some defect in the periodic structure. If radiation of frequency corresponding to the photonic band gap is then introduced to a point defect, the field will be trapped inside the defect since the propagation is prohibited inside the crystal. This effect can be exploited to design cavity resonators. The same effect can be used to create waveguides by introducing linear defects which can confine and guide the radiation without loss in the preferred path.

Another important application of photonic crystals is their ability to have lasing close to the band-edge because of the anomalous reduction of group velocity near the band-edge which induces an enhanced spontaneous emission thereby reducing the threshold for lasing. There had been several investigations in this direction [6].

Recently, along with the periodic photonic crystals, photonic band-gap materials with quasicrystal ordering are also been studied due to their peculiar properties. The following sections will discuss the important characteristics of quasiperiodic order and how they can be used for photonic applications.

## 1. Quasiperiodic order

The traditional division of structure of solids include crystals and amorphous materials (glassy). Crystals have their atoms arranged periodically with long-range translational symmetry. They also possess orientational order according to a particular crystallographic rotational symmetry. An amorphous material, on the contrary has the atoms densely packed, but randomly.

In 1984, D.Shechtman et al [7] experimentally observed a new class of 'ordering' in solids, when they found metallic solid (Al-14-at. %-Mn) with long-range orientational order, with icosahedral point group symmetry, which is inconsistent with lattice translations. The diffraction spots were as sharp as that of a crystal, but could not be indexed to any Bravais lattice. Even before the experimental observation of existence such 'quasi periodic' order in the microscopic level, similar quasiperiodic tilings were familiar from medieval times. Roger Penrose is a pioneer in the study of aperiodic tiling for planes, who proposed a set of two tiles (later referred to as Penrose tiling), that produced only non-periodic tilings of the plane.

The basic properties of quasicrystal structures are:

1. Quasiperiodic translational order: The density function is quasi periodic, which can be expressed as the sum of periodic function with at least some of the periods incommensurate. The rank of the Fourier module (the number of base vectors) exceeds the dimensionality of the structure. This makes the reciprocal space filled with diffraction peaks and the Fourier spectrum is singular continuous.

2. Minimal separation between atoms: in each quasicrystal lattice, the separation between any two nearest-neighbour sites lies between two characteristic distances $r$ and $R$ (both greater than zero). This distinguishes the quasicrystal from a set of sites obtained by superimposing two periodic lattices with periods whose ratio is irrational. This property makes quasicrystals different from a set of randomly arranged points.

3. Orientaional order: This is one of the key properties of a quasicrystal. The bond angles between neighbouring atoms or clusters have long range correlations and are oriented along a set of "star" axes that define the orientational order. Quasiperiodicity alone is not enough to characterize a quasicrystal since there are other physical systems like

incommensurate crystals are characterized by incommensurate periodicities. Non crystallographic orientational order not only differentiates quasicrystal from periodic and incommensurate crystals, but also forces quasiperiodicity. The set of irrational numbers that characterizes quasiperiodicty is constrained by the orientational symmetry whenever the symmetry is no-crystallographic.

The above mentioned properties make the quasicrystals different from amorphous or crystalline state of matter. The quasiperiodicty differenciates quasicrystals from periodic crystals where as the long-range orientational order makes them different from the amorphous solids like glass.

## 2. Generation of Quasicrystals

There are several methods to obtain quasicrystal geometries which have the properties described above.

### 2.1. Generalized dual-grid or multi-grid method

This is the straightforward formal approach for obtaining quasicrystals with arbitrary orientational symmetry. A grid refers to a countable infinite set of infinite non –intersecting curves (in 2-dim) or surfaces (3-dim). Inn two dimensions, *N*-grid is a set of N grids such that each curve in the $i^{th}$ grid intersects each curve in the $j^{th}$ curve at exactly one point for $i \neq j$. In three dimensions, *N*-grid is a set of N grids such that any triplets of surfaces in the ith, jth and kth grids, respectively (for $i \neq j \neq k$) intersect at exactly one point. A quasi lattice is then formed by the set of points lying in the intersection of a special class of *N*-grid which satisfies the properties such as quasiperiodic translational symmetry, orientational symmetry and finite number of Voronoi cell shapes This method is a numerically simple method for generating quasilattices with arbitrary symmetry, and for any given symmetry it creates the widest class of unit cell packings.

## 2.2. Direct quasiperiodic space tiling procedures

While considering the generation of quasicrystal, self-similarity is one of the interesting properties. When a structure is self-similar, the deflation/inflation operations can be used to transform the structure into itself within rescaling effects. One of the well-known examples for this procedure is the one-dimensional Fibonacci chain, which transforms into another Fibonacci chain with different tile sizes by using the substitution rule $L \rightarrow LS$ and$S \rightarrow L$. Thus starting with the single line segment L and repeating the deflation, a Fibonacci chain containing an arbitrarily large number of points can be generated. The 2-dimensional Penrose lattice can also be generated using inflation-deflation procedures.

Even though quasiperiodic structures are self-similar, self similarity does not ensure quasiperiodicity. So, a set of given tilings is not sufficient to generate a quasilattice. In order to force quasiperiodicity, one needs matching rules. The matching rules prescribe how neighbouring unit cells are allowed to match together in a quasilattice.

## 2.3. Quasiperiodicity as generated by projection or cut from higher dimensional space

The incompatible orientational symmetries associated with the quasiperiodic structures may be accepted by periodic tiling by increasing the dimensionality. In the strip projection method, the vertices of a *d*-dimensional rhombohedral packing are obtained by projection of points from a higher dimensional hypercubic lattice called parent lattice onto a *d*-dimensional hyper plane. The dimension of the parent lattice should be ≥ N, where N is the order of orientational symmetry. This method is geometrically simple and useful in analyzing the diffraction properties of the generated quasilattice.

In the 'cut projection method', the quasilattice is given by the intersection of a hyperplane (of dimension $d$) with the $N$-dimensional periodic (parent) lattice where N is the order of orientational symmetry. The vertices of the quasilattice are obtained from the intersections produced by "cutting" the hyper plane through the higher dimensional-lattice at a specified orientation.

## 2.4. Method of multiple beam interference

The interference of N coherent electromagnetic beams will result in a pattern which has an orientational symmetry equal to N. This method can be used to generate patters with quasiperiodic order and desired orientational symmetry.

In a typical experimental situation of $N$-beam interference [8], the irradiance profiles $I(\mathbf{r})$ achievable according to the relation

$$I(\mathbf{r}) = \sum_{m=1}^{N}\sum_{n=1}^{N} A_m A_n^{*} \exp[i(\mathbf{k}_m - \mathbf{k}_n)\cdot\mathbf{r} + i(\varphi_m - \varphi_n)],$$

where $A_m$, $\mathbf{k}_m$, $\varphi_m$, are the amplitudes, the wave vectors and the initial phases of the interfering beams, respectively, give quasiperiodic spatial distributions of the intensity maxima. The wave vectors $\mathbf{k}_m$ of the beams, for $m$=(1, …, $N$), are oriented, according to the following relation,

$$\mathbf{k}_m = \frac{2\pi n}{\lambda}\left(\sin\left(\frac{2\pi m}{N}\right)\sin\theta, \cos\left(\frac{2\pi m}{N}\right)\sin\theta, \cos\theta\right),$$

at angle $\theta$ with respect to the longitudinal direction along $z$-axis and are equally distributed along the transverse ($x$, $y$)-plane; $n$ is the average refractive index of the medium and $\lambda$ is the common wavelength of the beams. Usually, the beams are supposed having the same linear polarization. Their number $N$ is related to the rotational

symmetry of the quasicrystal [8]. By changing the phase retardation between the beams, different patterns having the same symmetry can be realized [8].

## 3. Types of quasicrystals

In this section, a few examples of quasicrystals geometries of different dimensionality are discussed.

### 3.1. One-dimensional QCs

One dimensional quasicrystals can be divided as follows:

**a) Fibonacci Sequence (FS)**

It is one of the most studied among the one dimensional quasicrystal structures and is determined by the substitution rule

$$L \to LS\ ,\ S \to L$$

Which can be written as $\sigma(L) = LS, \sigma(S) = L$, where $\sigma$ represents the substitution operator. This can also be represented in the matrix form as follows:

$$\sigma: \begin{pmatrix} L \\ S \end{pmatrix} \to \begin{pmatrix} 1 & 1 \\ 1 & 0 \end{pmatrix} \begin{pmatrix} L \\ S \end{pmatrix} = \begin{pmatrix} LS \\ L \end{pmatrix}$$

with $S = \begin{pmatrix} 1 & 1 \\ 1 & 0 \end{pmatrix}$ is the substitution matrix.

The eigen value equation corresponding to the above matrix is $\det|S - \lambda \boldsymbol{I}| = 0$, with $\boldsymbol{I}$ the unit matrix. The characteristic polynomial obtained by the evaluation of the above equation is $\lambda^2 - \lambda - 1 = 0$. The roots of this gives the eigen values of the substitution matrix as,

$$\lambda_1 = \frac{1+\sqrt{5}}{2} = \tau \text{ and } \lambda_2 = \frac{1-\sqrt{5}}{2} = \frac{-1}{\tau}$$

These eigen values satisfy the necessary condition (Pisot-Vijayaraghavan property) for having a Bragg component in the in the spectrum [4] because one of the eigen value is greater than 1, while the modulus of its conjugate is smaller than 1, i.e., $\lambda_1 > 1, |\lambda_2| < 1$.

The Fourier module of Fibonacci Series is of rank 2 and its diffraction pattern is purel point spectrum. There were several theoretical and experimental investigations on the properties of Fibonacci quasicrystals [5]. It was demonstrated that real band gaps can be formed in non-periodic structures [9].

**b) Non-Fibonacci aperiodic sequences**

Various aperiodic sequences can be generated by using different substitution matrix and initial conditions. One example is the well-known Thue-Morse sequence which is based on a two-letter alphabet ($L$,$S$) and the substitution rule $\sigma(L) = LS, \sigma(S) = SL$, which can be written as:

$$\sigma: \begin{pmatrix} L \\ S \end{pmatrix} \rightarrow \begin{pmatrix} 1 & 1 \\ 1 & 1 \end{pmatrix} \begin{pmatrix} L \\ S \end{pmatrix} = \begin{pmatrix} LS \\ SL \end{pmatrix}$$

The eigen value equation leads to characteristic polynomial $\lambda^2 - 2\lambda = 0$, which leads to the eigen values $\lambda_1 = 2$ and $\lambda_{12} = 0$. Although these numbers have Pisot-Vijayaraghavan property, the Fourier spectrum of the Thue-Morse is singular continuous without Bragg peaks. So, Thue-Morse sequence is not quasiperiodic and does not have a Fourier module.

Period-doubling sequence is another aperiodic sequence studied. It is also based on a two-letter alphabet ($L$, $S$) and the substitution rule $\sigma(L) = LS, \sigma(S) = LL$. This can be expressed in the matrix form as the following:

$$\sigma: \begin{pmatrix} L \\ S \end{pmatrix} \rightarrow \begin{pmatrix} 1 & 1 \\ 2 & 0 \end{pmatrix} \begin{pmatrix} L \\ S \end{pmatrix} = \begin{pmatrix} LS \\ LL \end{pmatrix}$$

The characteristic equation is $\lambda^2 - \lambda - 2 = 0$ which gives the eigen values $\lambda_1 = 2$ and $\lambda_2 = -1$. These values do not have the Pisot-Vijayaraghavan property and the Fourier module is of infinite rank. The Fourier spectrum is pure point and the sequence is almost periodic.

Rudin-Shapiro sequence in an aperiodic sequence based on a four-letter alphabet (*A*, *B*, *C*, *D*) and the substitution rules $\sigma(A) = AB, \sigma(B) = AC, \sigma(C) = DB$ and $\sigma(D) = DC$.

$$\sigma: \begin{pmatrix} A \\ B \\ C \\ D \end{pmatrix} \rightarrow \begin{pmatrix} 1 & 1 & 0 & 0 \\ 1 & 0 & 1 & 0 \\ 0 & 1 & 0 & 1 \\ 0 & 0 & 1 & 1 \end{pmatrix} \begin{pmatrix} A \\ B \\ C \\ D \end{pmatrix} = \begin{pmatrix} AB \\ AC \\ DB \\ DC \end{pmatrix}$$

The corresponding eigen values are $\lambda_1 = 0, \lambda_2 = 2\lambda_3 = \sqrt{2}$ and $\lambda_4 = -\sqrt{2}$, which do not show the Pisot-Vijayaraghavan property. The Fourier spectrum of this sequence is absolutely continuous and therefore does not have a Fourier module. Only a few studies have been done on these structures.

## 3.2. Two-dimensional Quasicrystals

When the quasiperiodic translational order is extended to two and three dimensions, orientational symmetry comes into play. Just as discussed before, the quasiperiodicity is forced by certain orientational symmetries. Just as in the case of periodic crystal, where the periodicity is allowed only for certain orientations, quasiperiodicity is also allowed only for certain orientational symmetries. When quasicrystals possess the crystallographic orientational symmetries, they are called incommensurate crystals. But in this case, the orientational symmetry does not force the quasiperiodicity and orientational symmetry and quasiperiodicity are totally decoupled. Quasiperiodic structures with non-crystal orientational symmetries are more interesting. In this section, some of the well-known quasicrystal structures are discussed.

**a) 8-fold symmetry**

One of the most commonly used quasicrystal patterns is 8-fold symmetric pattern with Ammann-Beenker tiling. Decorated Ammann-Beenker tiles are two rhombi with acute angles 45° and a square, and lengths of their edges are the same. Two methods can be used to generate structures with this tiling. One is the substitution method which has two phases; the tiles are expanded and then the new tiles are replaced by patches of the original tiles. This can be repeated giving larger patches of tiling. The second method is to construct the tiling as a planar slice of a four dimensional lattice and then project this to the plane (cut and project method). Figure 1 shows an example of Ammann-Beenker tiled 2-dimensional quasicrystal.

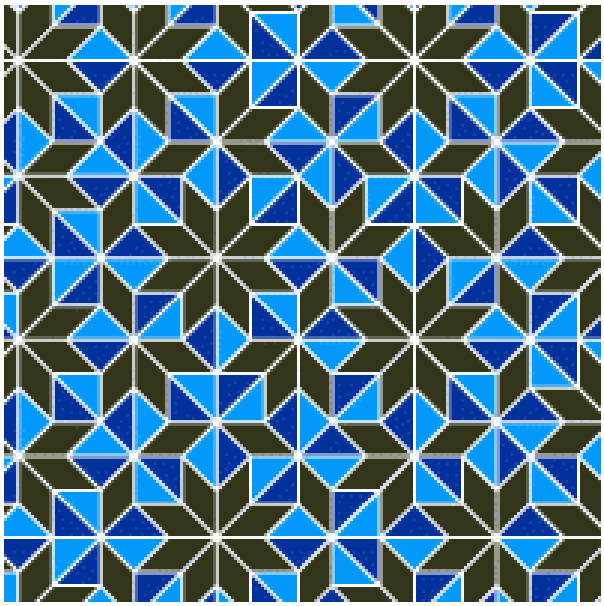

***Figure.1.1. 2-D Amman-Beenker tiling with 8-fold symmetry***

**b) 10-fold symmetry**

Penrose tiling [10] is one of the most famous and well-studied among the 2-dimensional quasicrystals. There are different kinds of Penrose tilings all of which have 10-dimensional orientational symmetry of the

diffraction images called the 'decagonal phase' . The penrose tiling shown in figure (1.2) consists of rhombuses of two kinds with the acute angle to either $2\pi/10$ or $2\pi/5$. Any of the three following methods can be used to generate the Penrose tiling:

i) Matching rules for the thick and thin rhombuses
ii) The cut and project scheme from a periodic lattice in a five-dimensional hyperspace
iii) Dual grid techniques

In the case of dual multi-grid technique, a regular star formed by the set of five basic vectors is constructed as the starting point. These vectors are defined as

$$\boldsymbol{e}_n = \left[\cos\left(\frac{2\pi n}{5}\right), \sin\left(\frac{2\pi n}{5}\right)\right]$$

Where: $n$= 0,...,4

Then a grid is formed (as described in the earlier section) with five fold rotational symmetry whose dual transformation will give the desired Penrose lattice. Another method to produce a 10-fold symmetric structure is to use the optical interferometric method. An example for such a structure is shown in figure (1.2)

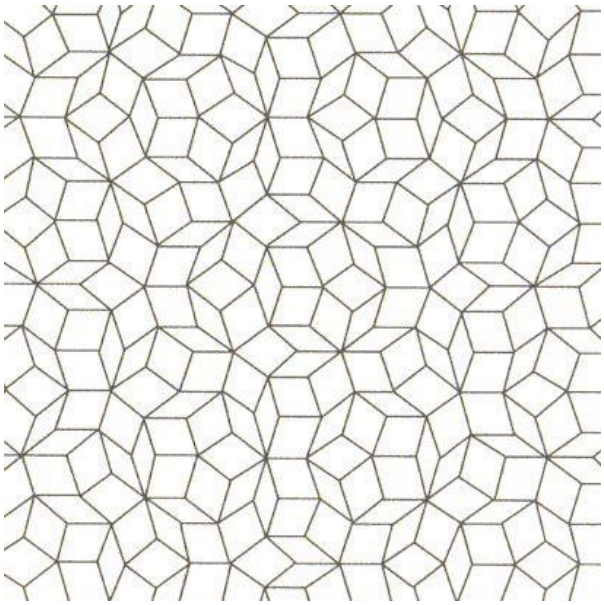

*Figure.1.2. 2-D 10-fold symmetric Penrose tiling*

### c) 12-fold symmetry

The most widely known 12-fold symmetric quasicrystal is dodecagonal tiling. It is formed by Stampfli inflation rule which has four steps as follows [10]:

1. Draw the parent regular dodecagon and decorate it with square-triangle tiling (Figure)
2. Scale the parent dodecagon by a factor of $1/(2+\sqrt{3}) \approx 0.27$ to obtain the offspring-dodecagon of the type I. The type II dodecagon is obtained by rotation of dodecagon I by an angle π/6.
3. Place the offspring dodecagons on each vertex of the parent one.
4. Repeat the steps 2 and 3 for the structure obtained in step 3 as the new parent tiling.

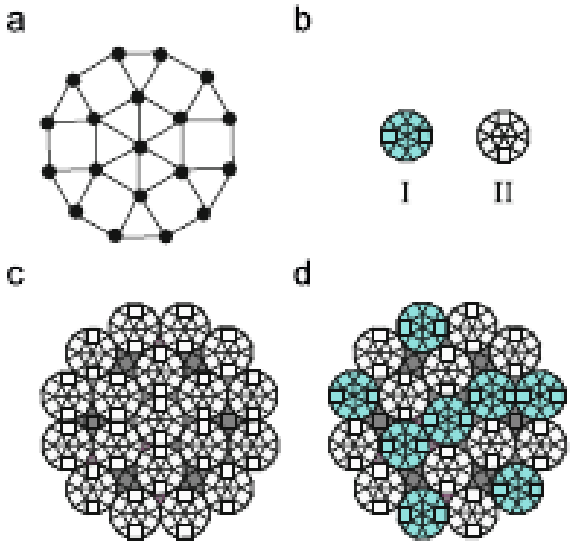


**Figure.1.3. Formation of dodecagonal crystal by inflation rule: (a) the parent tiling (b) offspring dodecagons (c) and (d) resulting dodecagons after iteration (A.N. Poddubny et al)**

Several reports have been published about the generation 12-fold symmetric quasicrystals using various methods, including the method of optical interference [11]

Lately, there are investigations on quasicrystals of even higher symmetries like 17- and 23-fold [8]

### 3.3 Three-dimensional quasicrystals

The most studied 3-dimensional quasicrystal is the icosahedral quasicrystal, which was observed to be naturally occurring in the Al-Mn alloy. The simplest set of unit cell shapes for the icosahedral quasicrystal consists of the oblate and prolate rhombohedra. The matching and deflation rules applied to the rhombohedra are much more complicated than the two-dimensional analogues. Two rhombohedra with the same shape can have different matching and deflation rules.

## 4. Quasicrystals for photonic applications

The discovery of quasicrystals led to the use of this new class of ordered structures also for photonic applications. Despite being aperiodic, quasicrystals can possess a photonic band gap just like a periodic photonic crystal [12]. But quasicrystals also have peculiar properties such as non-crystallographic, higher order orientational symmetry and defect-free localization [13].

The first reports on the evidence of a photonic band-gap in aperiodic heterostructures based on one dimensional Fibonacci sequence were from Merlin *et al* [14]. The one dimensional quasicrystals are realized by stacking layers of two different dielectric materials according to the specific generation rule. Apart from having a photonic band-gap, the Fibonacci quasicrystals have also reported to have self-similar energy spectrum [15] and critically localized states. The luminescence properties of an active Fibonacci quasicrystal are studied by V.Passais *et al* [16]. The photoluminescence (PL) studies on these structures demonstrated faster radiative decay rate due to the large photon density of states available at the edge of the pseudo-bandgap due to the

presence of critically localized states. One dimensional photonic structures based on Thue-Morse sequence also have shown to have omnidirectional band gap for both TE (transverse electric) and TM (transverse magnetic) polarizations when the refractive index contrast is sufficiently high [17].

Several two dimensional quasiperiodic geometries have been studied to understand the formation and properties of band gap, presence of localized states and their applications. Two dimensional quasicrystals can be realized by either placing dielectric cylinders or by having holes made in a dielectric material at the vertices of tiles corresponding to the desired geometry. The first studies on two-dimensional photonic quasicrystals were done by Chan *et al* [18]. They investigated the transmission properties of an 8-fold symmetric PQC and theoretically demonstrated the existence of a photonic band gap in it. The dependence of the band gap on the filling fraction, the dielectric constant and angle of incidence octagonal quasicrystals also have been investigated [30]. Numerical studies by J. Romero-Vivas et al showed that the octagonal quasicrystal can possess a photonic band-gap for refractive index contrasts as low as 0.26 for the TM polarization [19]. They also studied the properties of optical microcavity and waveguides realized using the 8-fold symmetric PQC, which can be used to design an add-drop filter.

A detailed analysis of the diffraction properties and band structure formation in Penrose-tiled 10-fold symmetric PQC is done by M.A. Kaliteevski *et al* [20]. A.Della Villa *et al* investigated the properties of resonant modes occurring in the transparency bands of finite-sized Penrose-type PQCs [21]. These defect-free localized states are shown to be the inherent property of quasicrystals. Y. Neve-Oz *et al* showed the possibility of achieving fast light in a metamaterial realized using the Penrose quasicrystal geometry [22]. They demonstrated the presence of the presence of the band gap edge states that are characterized by a

very small refractive index. Organic laser based on Penrose-tiled PQCs was also demonstrated [23].

Dodecagonal quasicrystals are acquired attention because of their higher order of rotational symmetry and thus the possibility to possess more isotropic band gaps. Localization of cluster resonance is observed in 12-fold symmetric PQCs were first reported by Wang *et al* [24]. Formation of complete PBG in 12-fold symmetric dodecagonal PQC was numerically and experimentally studied by Zoorob *et al* [12]. Dodecagonal quasicrystals also reported to have focusing properties [25]. The evidence of directive low-sidelobe emission of radiation from embedded line source in finite-sized, defect-free 12-fold symmetric quasicrystals was given by the numerical analysis done by A.Micco *et al* [26].The photonic band-gap properties of 12-fold symmetric quasi-crystal patterns formed by double-beam multiple exposure holography was studied theoretically by Gauthier et al [11].

## 5. Fabrication methods for photonic quasicrystals

Fabrication of two- and three-dimensional quasicrystals is not a trivial task because of their structural peculiarities. It is difficult or almost impossible (especially for the 3-dimensionl PQCs) to use the usual methods used in the fabrication of periodic quasicrystals such as the self-assembly of colloidal microspheres, micro fabrication or semiconductor lithography for the fabrication of PQCs. Method of optical interference lithography (multi-beam hololithography or holographic lithography) is a versatile method and is found to be very useful for the fabrication of both PQCs and PCs [27]. This method can be used to realize quasicrystals in mesoscale PQCs in photosensitive media.

Holographic lithography is based on optical interference of two or more beams. The photosensitive material is exposed to the generated interference pattern. In most of the cases multiple exposures will be necessary [13]. The coherent laser beams are usually obtained by splitting the single laser beam using suitable gratings, prisms or dielectric beam splitters [28]. The photosensitive material having the structure of the interference pattern can be used as a mask or infiltration template after developing. The shape of the dielectric region and thus the filling fraction can vary depending on the exposure time. In principle, this method can be used to fabricate PQCs of very higher order of rotational symmetry since the order symmetry of an interference pattern depends on the number of interfering beams. But experimentally it becomes very difficult, if not impossible to control the phase and amplitude of a large number of coherent laser beams. An approach to overcome this difficulty is to use dual-beam multiple exposure holography [11]. Gauthier *et al* described the generation of 12-fold symmetric PQC patterns using six equal-duration exposures of the photosensitive sample with the sample rotated in the film plane by 30° between exposures. Even this method can be really tedious since it requires precise mechanical control over the rotation. The best way to overcome these difficulties is to have a technique which uses minimum a number of laser beams and can write the pattern in a single step.

A method for single-beams holographic lithography was demonstrated by Yang *et al* [29]. They fabricated PQCs of various higher-order rotational symmetries using a single beam by adjusting the phase relation of interference beams through an optical mask. Another simpler method is to combine computer generated holography with programmable spatial light modulators (SLM) [8]. Using this method two-dimensional or even three-dimensional spatial distribution of optical beams of almost any kind can be created. This also allows the fabrication of patterns such as Thue-Morse which cannot be generated

using the theory of multiple beam interference. This technique is explained in more detail in Chapter 4. Other methods for fabrication of quasicrystals include direct laser writing [30] and laser focused atomic deposition [31].

# Chapter 2

# Background theory and FDTD simulations

Photonic band-gap is the most interesting property of both photonic crystals and photonic quasicrystals. It is important to understand how photonic band gap is formed in these structures. If we know the parameters which determine the properties of photonic band-gap, it is easier to engineer the band gap for specific applications. The electromagnetic theory can be applied to these 'meta-crystals' to understand how these materials respond to the electromagnetic radiation.

## 1. Electromagnetism of photonic crystals

In order to understand the formation of photonic band gap in photonic crystals, it is necessary to analyze the propagation of electromagnetic energy in a complex dielectric medium, which can be done by using the macroscopic Maxwell equations.

The four macroscopic Maxwell equations in SI units are;

$$\nabla . \boldsymbol{B} = 0 \qquad \nabla \times \boldsymbol{E} + \frac{\partial \boldsymbol{B}}{\partial t} = 0$$
$$\nabla . \boldsymbol{D} = \rho \qquad \nabla \times \boldsymbol{H} - \frac{\partial \boldsymbol{D}}{\partial t} = \boldsymbol{J} \tag{2.1}$$

Where E and H are the macroscopic electric and magnetic fields, D and B are the displacement and magnetic induction fields, ρ and J are the free charge and current densities respectively.

If we consider that the electromagnetic field is propagated within a medium of mixed dielectric materials (the dielectric constant is a

function of the position vector $\boldsymbol{r}$), in which the structure is time-invariant, we can take $\rho = 0$, $\boldsymbol{J} = 0$ since there are no free charges or currents.

The electric field **E** can be related to the displacement **D** through $\mathbf{D}(\boldsymbol{r}) = \varepsilon_0 \varepsilon(\boldsymbol{r})\mathbf{E}(\boldsymbol{r})$ if the following assumptions are taken:

1. The field strength is small enough so that the higher order susceptibilities are negligible. This implies that non-linear effects are not taken into account.

2. The material is macroscopic and isotropic so that $\mathbf{E}(\boldsymbol{r},\omega)$ and $\mathbf{D}(\boldsymbol{r},\omega)$ are related through $\varepsilon_0$ multiplied by a scalar dielectric function $\boldsymbol{\varepsilon}(\boldsymbol{r},\omega)$ that is also called the relative permittivity.

3. The material dispersion is ignored, which means the dielectric constant of the material does not have any explicit dependence on the frequency of the radiation.

4. The materials are considered to be transparent to the electromagnetic radiation at the particular frequency range considered, such that the relative permittivity can be treated as purely real and positive.

These assumptions also allow to have the relation $\mathbf{B}(\boldsymbol{r}) = \mu_0 \mu(\boldsymbol{r})\mathbf{H}(\boldsymbol{r})$ in the case of magnetic field, the vacuum permeability $\mu_0 = 4\pi \times 10^{-7}$ Henry/m. For most of the dielectric materials, the value of the relative permeability $\mu(\boldsymbol{r})$ is close to unity, which makes $\mathbf{B} = \mu_0 \mathbf{H}$.

With all the above assumptions, the Maxwell equations can be written as:

$$\nabla . \mathbf{H}(\boldsymbol{r},t) = 0 \qquad \nabla \times \mathbf{E}(\boldsymbol{r},t) + \mu_0 \frac{\partial \mathbf{H}(\boldsymbol{r},t)}{\partial t} = 0 \tag{2.2}$$

$$\nabla.[\varepsilon(\boldsymbol{r})\,\mathbf{E}(\boldsymbol{r},t)] = 0 \qquad \nabla \times \mathbf{H}(\boldsymbol{r},t) - \varepsilon_0 \varepsilon(\boldsymbol{r}) \frac{\partial \mathbf{E}(\boldsymbol{r},t)}{\partial t} = 0$$

Although **E** and **H** are complicated functions of both time and space, using the linearity of Maxwell equations we can separate the time dependence from the space dependence by expanding the fields into a set of harmonic modes. So we can express the fields as follows

$$\mathbf{H}(\boldsymbol{r},t) = \mathbf{H}(\boldsymbol{r})e^{-i\omega t}$$

$$\mathbf{E}(\boldsymbol{r},t) = \mathbf{E}(\boldsymbol{r})e^{-i\omega t} \tag{2.3}$$

Substituting the above equations in (2.2) makes the divergence equations as follows:

$$\nabla.\mathbf{H}(\boldsymbol{r}) = 0 \tag{2.4a}$$

$$\nabla.[\varepsilon(\boldsymbol{r})\,\mathbf{E}(\boldsymbol{r})] = 0 \tag{2.4b}$$

The physical interpretation of (2.4) is that there are no point sources or sinks of the induction field and displacement field within the medium.

The curl equations in (2.2) become:

$$\nabla \times \mathbf{E}(\boldsymbol{r}) - i\omega\mu_0\,\mathbf{H}(\boldsymbol{r}) = 0 \tag{2.5a}$$

$$\nabla \times \mathbf{H}(\boldsymbol{r}) + i\omega\varepsilon_0\varepsilon(\boldsymbol{r})\mathbf{E}(\boldsymbol{r}) = 0 \tag{2.5b}$$

These equations can be decoupled by eliminating the electric filed using the equation (2.5a) which results in an equation entirely in $\mathbf{H}(\boldsymbol{r})$.

$$\nabla \times \left(\frac{1}{\varepsilon(\boldsymbol{r})}\nabla \times \mathbf{H}(\boldsymbol{r})\right) = \left(\frac{\omega}{c}\right)^2 \mathbf{H}(\boldsymbol{r}) \tag{2.6}$$

The above equation can provide the complete information about $\mathbf{H}(\boldsymbol{r})$ together with (2.4 a). Once the spatial profile of the dielectric constant

of the medium ($\varepsilon(\boldsymbol{r})$) is known, (2.6) can be solved to get the harmonic modes $\mathbf{H}(\boldsymbol{r})$ for a given frequency subject to the divergence condition with the known boundary conditions. Then the electric filed can be deduced by using (2.5b)

$$\mathbf{E}(\boldsymbol{r}) = \left[\frac{i}{\omega\varepsilon_0\varepsilon(\boldsymbol{r})}\right]\nabla \times \mathbf{H}(\boldsymbol{r}) \tag{2.7}$$

This also makes sure that the electric field satisfies the transversality condition $\nabla.\varepsilon\mathbf{E} = 0$, since the divergence of a curl is always zero.

Equation (2.6) is in the form of an eigen value equation which can be expressed as

$$\Theta\,\mathbf{H}(\boldsymbol{r}) = \left(\frac{\omega}{c}\right)^2 \mathbf{H}(\boldsymbol{r}) \tag{2.8}$$

where $\Theta$ is the Hermitian operator , $\mathbf{H}(\boldsymbol{r})$ are the eigen vectors and $\left(\frac{\omega}{c}\right)^2$ is the eigen value. $\mathbf{H}(\boldsymbol{r})$ gives the spatial pattern of the harmonic modes and the eigen values $\left(\frac{\omega}{c}\right)^2$ are proportional to the squared frequencies of those modes. In the case of a periodic photonic crystal, the dielectric constant can be expressed as $\varepsilon_k(\boldsymbol{r}) = \varepsilon_k(\boldsymbol{r}+\boldsymbol{R})$, varying in the direction *k*. Using this relation one can obtain the band-structure of the photonic crystals.

Evoking the analogy with quantum mechanics, equation (2.8) reveals several interesting and useful properties of Maxwell equations:

1. Since the operator $\Theta$ is Hermitian, the corresponding eigen values are orthogonal.

2. The field solutions to the time-dependent form of the equation (2.8) ;

$$\Theta\,\mathbf{H}(\boldsymbol{r},\mathrm{t}) = -\frac{\partial^2\,\mathbf{H}(\boldsymbol{r},\mathrm{t})}{\partial t^2} \tag{2.9}$$

should have a spectral decomposition in terms of the eigen vectors of (2.8) with appropriate time-dependent exponential coefficients.

3. The Hermitian nature of $\boldsymbol{\Theta}$ can be used to show that the eigen values of (2.8) are real as follows:

$$\boldsymbol{\Theta}\,\mathbf{H}(\boldsymbol{r}) = \left(\frac{\omega}{c}\right)^2 \mathbf{H}(\boldsymbol{r}) \tag{2.10a}$$

$$(\mathbf{H}\boldsymbol{\Theta}\,\mathbf{H}) = (\omega/c)^2(\mathbf{H},\mathbf{H}) \tag{2.10b}$$

$$(\mathbf{H}\boldsymbol{\Theta}\,\mathbf{H})^* = \left(\omega^2/c^2\right)^* (\mathbf{H},\mathbf{H}) \tag{2.10c}$$

Since $\mathbf{H}$ is Hermitian, $(\mathbf{H},\boldsymbol{\Theta}\,\mathbf{H}) = (\boldsymbol{\Theta}\,\mathbf{H},\mathbf{H})^*$ which implies that $\left(\omega^2/c^2\right)^* = \left(\omega^2/c^2\right)$, and since $c$ is real number, it follows that $(\omega^2)^* = \omega^2$ is real.

$$(\mathbf{H},\mathbf{H})(\omega/c)^2 = \int d^3r \frac{1}{\varepsilon(\boldsymbol{r})} |\nabla \times \mathbf{H}|^2 \tag{2.11}$$

Since ε(r) is positive everywhere, the eigen values must be non-negative indicating real $\omega$.

4. Another very important property of the Maxwell equation is its scale invariance, which means that the solution has the same form in all the length scales (assuming that the system is macroscopic). This property has an important technological role. Let us recall the master equation,

$$\nabla \times \left(\frac{1}{\varepsilon(\boldsymbol{r})} \nabla \times \mathbf{H}(\boldsymbol{r})\right) = \left(\frac{\omega}{c}\right)^2 \mathbf{H}(\boldsymbol{r}) \tag{2.12}$$

In order to see what happens to the harmonics with a different length scale, let us consider $\boldsymbol{r}' = s\boldsymbol{r}$, where the $\boldsymbol{r}$ length is scaled by a factor $s$. The equation according to the new length scale $\boldsymbol{r}'$ is as follows:

$$s\nabla' \times \left( \frac{1}{\varepsilon(\boldsymbol{r}'/s)} s\nabla' \times \mathbf{H}(\boldsymbol{r}'/s) \right) = \left(\frac{\omega}{c}\right)^2 \mathbf{H}(\boldsymbol{r}'/s) \tag{2.13}$$

$\varepsilon(\boldsymbol{r}'/s)$ is equivalent to $\varepsilon'(\boldsymbol{r}')$, which makes the above equation as follows;

$$\nabla' \times \left( \frac{1}{\varepsilon'(\boldsymbol{r}')} \nabla' \times \mathbf{H}(\boldsymbol{r}'/s) \right) = \left(\frac{\omega}{cs}\right)^2 \mathbf{H}(\boldsymbol{r}'/s) \tag{2.14}$$

This is the master equation itself with the new mode profile $\mathbf{H}(\boldsymbol{r}')$ and the frequency scaled to $(\omega' = {}^{\omega}/_{s})$. This means that the new mode profile and the corresponding frequency can be determined by rescaling the old mode profile and frequency. Once we solve the master equation for a particular length scale, it can be used to obtain the mode profiles for all other length scales of importance. This especially useful while studying the photonic structures which are difficult or even impossible to be fabricated in particular length scales due to practical difficulties.

## 2. Photonic band structures

In the case of periodic photonic crystals, the analogy with crystals can be used to calculate the band structure. As in the case of electronic waves in a crystal, the electromagnetic waves propagating inside a photonic crystal obey Bloch theorem. The modes of a three dimensional periodic system are Block states that can be labelled by a Bloch wave vector $\mathbf{k} = k_1\mathbf{b}_1 + k_2\mathbf{b}_2 + k_3\mathbf{b}_3$ where $\mathbf{k}$ is in the Brillouin zone (BZ). Each value of $\mathbf{k}$ inside the Brillouin zone corresponds to an eigen state of $\boldsymbol{\Theta}$ with frequency $\omega(\mathbf{k})$ and eigen vector $\mathbf{H}_\mathbf{k}$ of the form

$$\mathbf{H}_\mathbf{k}(\mathbf{r}) = e^{i\mathbf{k}.\mathbf{r}}\mathbf{u}_\mathbf{k}(\mathbf{r}) \tag{2.15}$$

where $\mathbf{u_k(r)}$ is a periodic function on the lattice : $\mathbf{u_k(r) = u_k(r+R)}$ for all lattice vectors **R**.

We can use the Bloch state in (2.15) in the master equation (2.10) which results in:

$$\Theta\, \mathbf{H_k(r)} = \left(\frac{\omega(\mathbf{k})}{c}\right)^2 \mathbf{H_k(r)} \tag{2.16}$$

$$\nabla \times \frac{1}{\varepsilon(\mathbf{r})} \nabla \times e^{i\mathbf{k}.\mathbf{r}} \mathbf{u_k(r)} = \left(\frac{\omega(\mathbf{k})}{c}\right)^2 e^{i\mathbf{k}.\mathbf{r}} \mathbf{u_k(r)} \tag{2.17}$$

$$(i\mathbf{k} + \nabla) \times \frac{1}{\varepsilon(\mathbf{r})} (i\mathbf{k} + \nabla) \times \mathbf{u_k(r)} = \left(\frac{\omega(\mathbf{k})}{c}\right)^2 \mathbf{u_k(r)} \tag{2.18}$$

$$\Theta_{\mathbf{k}} \mathbf{u_k(r)} = \left(\frac{\omega(\mathbf{k})}{c}\right)^2 \mathbf{u_k(r)} \tag{2.19}$$

$\Theta_{\mathbf{k}}$ is the newly defined Hermitian operator which depends on **k**.

$$\Theta_{\mathbf{k}} \triangleq (i\mathbf{k} + \nabla) \times \frac{1}{\varepsilon(\mathbf{r})} (i\mathbf{k} + \nabla) \times \tag{2.20}$$

The eigen value problem (2.19) can be solved to get the function **u** and the mode profiles by applying the periodicity condition $\mathbf{u_k(r) = u_k(r+R)}$ and subject to the transversality condition $(i\mathbf{k} + \nabla).\mathbf{u_k} = 0$. The periodic boundary condition helps to reduce the eigen value problem to a single unit cell of the photonic crystal. The solution of (2.19) leads to the description of modes supported by a photonic crystal. They are the family of continuous functions $\omega_n(\mathbf{k})$, indexed in the order of increasing frequency by the band number. This information obtained from this

band structure helps us to deeply understand the optical properties of the photonic crystals.

Two different mechanisms contribute to the formation of band gap in photonic meta-crystals. First one is the Bragg-scattering mechanism which is better understood by taking the analogy with a nearly free electron system and resonance mechanism analogous to the tight binding approach. Bragg scattering happens when the wave vector of the incident radiation points to the boundary of a Brillouin zone. When this condition is satisfied, the waves are reflected by certain scatterers. The back scattered waves interact with the incident waves to generate standing waves which leads to the splitting of the dispersion relation. Another mechanism of band gap formation is Mie resonances. In this case the structure is considered as a tight-bound system of *N* single resonators. If they are all independent, the resonance frequency is the same for all of them ($\omega_{res}$). In case of interaction, a state of *N*-fold degeneracy is formed around $\omega_{res}$. This resonance frequency is structure independent and usually depends on the shape of the scatterers. In general, the band-gap in the photonic structure is a result of overlapping of these two regimes of scattering. The different computational techniques described in the following section also use either or both of these mechanisms while calculating the band gap properties of the systems.

In the case of quasicrystalline structures, the description of Bragg scattering needs description of an 'induced' periodicity. The photonic band gap of these structures also reflects their scaling symmetry and self-similarity [18]. Another important feature of the PQC band gap is that they can possess both extended- and critically-localized modes together [18].When it comes to quasicrystals, the lack of periodicity and of the unit cell makes it impossible to define a Brillouin zone. One approach is to introduce an artificial periodicity (super cell

approximation) whereas the second method is to consider the finite structure.

Powerful computational techniques are required to calculate the transmission properties of both photonic crystals and quasicrystals. It is very important to have computer programs which can give quite accurate results so that we can predict the behaviour of the photonic crystals/quasicrystals before they are fabricated. In the following section some of the computational techniques are described.

## 3. Common techniques in Computational photonics

Depending on the approach used for calculation, computational methods can be broadly divided into three categories.

- Frequency domain eigen problems: solves the Maxwell eigen problem for the given frequencies in a periodic system. The generalized form of the eigen value equation in the form of $Ax = \omega^2 Bx$ where $A$ and $B$ are $N \times N$ matrices and $x$ is the eigen vector. $A$ and $B$ are Hermitian and $B$ is positive definite (since the problem is Hermitian). The eigen values and eigen vectors can be found out using linear algebra.
- Frequency domain responses: this method is particularly useful to estimate the transmission and reflection through a finite structure from a given source at a given frequency. In this method, the field resulting by a given current distribution at a fixed frequency is estimated by expressing the problem as a finite matrix equation $Ax = b$ and applying linear algebra techniques to solve it.
- Time domain simulations: they present the most general approach by solving the time dependent Maxwell equations, propagating the fields in both time and space. Usually the solver simulate the fields $\mathbf{E}(\boldsymbol{x},t)$ and $\mathbf{H}(\boldsymbol{x},t)$ starting from a current

source $\mathbf{J}(\boldsymbol{x},t)$. Since it also takes into account of the time variation of the fields, this method can also be used to simulate optically active or non-linear media.

Now let us see some of the most common numerical methods used to study properties of photonic crystals and quasicrystals.

## 3.1. Plane wave method

In the plane wave expansion technique, the dispersion relation is calculated based on the expansion of wave field in terms of plane waves to find the eigen states of the Maxwell equations. This is done by taking into account of the Bloch theorem, which is applicable only for periodic crystals. In an infinite periodic photonic crystal, using Bloch theorem, a mode in a periodic structure can be expanded as a sum of infinite number of plane waves as follows:

$$\mathbf{H}(\boldsymbol{r}) = \sum_{G,\lambda} h_{G,\lambda}\, \hat{e}_{\lambda} e^{i(\vec{k}+\vec{G}).r} \tag{2.21}$$

where λ=1, 2, $\vec{k}$ is the wave vector of the plane wave, $\vec{G}$ is the reciprocal lattice vector, $\hat{e}_{\lambda}$ represents the two unit axis perpendicular to the propagation direction $\vec{k}+\vec{G}$.

Using this expression in the standard Maxwell equation, we obtain a Helmholtz equation that can be solved easily with linear algebra. This method is very powerful in obtaining the band diagram of the crystal concerned. But it also has some drawbacks.

As mentioned above, this method is applicable only for periodic crystals. So this method is not directly applicable to aperiodic geometries such as quasicrystals. This method has been used to analyze the band-diagram of quasicrystals by using their periodic approximants [32]. Another issue is that the plane wave expansion in (2.21) is

applicable for infinite crystal. So, when it comes to the analysis of finite structures (which is the case for most of the experimentally realized structures), the calculations become cumbersome.

## 3.2. Transfer Matrix Method (TMM)

The basic formalism of TMM yields the amplitude of the electromagnetic field of monochromatic waves reflected by and transmitted through crystal structure. The solution is achieved through propagation of the fields in the homogeneous layers, and the continuity of the tangential components of the electric and magnetic fields at the interfaces. This method has different methods of implementation. The common factor in all of them is that a matrix, which relates the fields on one boundary to those on another, is somehow created. This method is particularly useful in solving the photonic crystal slab problems. Different methods are used to expand the fields in TMM such as finite differences or finite elements [33], plane waves [34-35], eigenvectors. This method readily gives the reflection and transmission coefficients of a system. The main disadvantage of using this technique is that sometimes it leads to numerical instabilities.

## 3.3. Multiple scattering method

The multiple scattering approach is based on preliminary calculation of the scattering behaviour of single scattering objects. It uses the analytically calculated scatter matrix of each element in the system and the recursive use of addition theorem of harmonics to calculate the scatter matrix corresponding to the whole system. If the individual scatterers are spherical or cylindrical, it is easy to obtain the scatter matrix analytically. Once the scatter matrices are known, further calculations are quite easy. The advantage of this technique is that it can be used for both 2-D and 3-D crystals, either finite or infinite. This method requires that all particles, irrespective of their shapes, be

enclosed in non-overlapping circles (2-D) or spheres (3-D). This makes it impossible to obtain the properties of a lattice of particles of shapes other than circles (or spheres).

## 3.4. Finite difference time domain method (FDTD)

As the name implies the FDTD method divides space and time into grids of discrete points and approximates the derivatives of the Maxwell equations by finite differences. The FDTD method is a rigorous solution to Maxwell equation and does not have any approximations or theoretical restrictions. The FDTD method solves Maxwell equations by first discretizing the equation via central differences in time and space and then numerically solving the equations.

The most common method used to solve the Maxwell equations is based on the Yee's mesh. Time is broken into discrete steps of $\Delta t$. The electric field components are then calculated at times $t = n\Delta t$ and the magnetic displacement field (***H***) at t $= \left(n + {}^{1}/_{2}\right)\Delta t$ , where $n$ is represents the computational step. ***E*** and ***H*** fields are marched through time, having an offset of half of the time step $\Delta t$. This method results in equations that can be used to compute the fields at a given mesh point by iteratively solving them in a leapfrog manner, alternating between computing the ***E*** and ***H*** fields at subsequent $\Delta t/2$ intervals.

FDTD algorithms can be employed to compute various properties of the optical system. For example, the field pattern resulting from a localized source at a particular frequency can be easily calculated; which is given by the Green's function of the system. Another most common use of the FDTD method is to compute the transmission or reflection spectra of a given finite structure in response to some stimulus. Unlike the frequency domain solvers, the time domain methods can provide the response of the system for many different frequencies in a single

computation. This is done by taking the Fourier transform of the response obtained by applying a single short-time pulse. However, from a computational point of view this of cause requires a longer time. FDTD method can also be used to calculate the resonant or eigen modes of a given structure. Band structures can also be computed using this method by imposing the Bloch-periodic boundary condition. The largest disadvantage of FDTD method is that it requires long-time simulations to obtain the required results.

## 4. Results of simulations using FDTD method

In this section, simulation results showing some interesting transmission properties of photonic quasicrystals are presented.

Using FDTD simulations, the transmittance spectra of eight-, ten- and twelve-fold quasicrystal structures are calculated. Two different quasiperiodic spatial patterns of tiling are considered and compared for each fixed rotational symmetry. It is shown how different quasi-lattice tiles dramatically affect the photonic band-gap properties for low refractive index contrasts, demonstrating the importance of the tiling geometry in the arrangement of a quasicrystal structure. If wide PBGs are to be obtained at low index contrast, the particular tiling pattern is more important than symmetry and, hence, very accurate control of the fabrication parameters is mandatory in order to produce quasicrystals possessing the PBG properties needed for feasible and reliable photonic applications.

### 4.1. Quasicrystal design and simulations

As described in the first chapter, there are several quasicrystal geometries which are being studied. In this section, two different patterns each of non-periodic spatial tiling for two-dimensional (2D) symmetric quasi-lattices with octagonal (8-fold), decagonal (10-fold) and dodecagonal (12-fold) point group are studied.

Recently, holographic techniques based on interferential schemes have been widely employed to fabricate PQCs with high rotational symmetries [36-37]. The light distribution obtained from the interference of two or many coherent light beams is transferred to a photosensitive medium producing the desired quasiperiodic dielectric modulation by single or multiple exposure process. The scattering centres (typically rods in a binary pattern) of the quasi-lattice correspond to the maxima positions of the light distribution resulting from the N-beam interference. The rotational symmetry is determined by the number of beams, while the particular tiling pattern of the structure depends on the light intensity, time exposure and on the delicate balance among direction, polarization, amplitude and phase of the beams. By controlling the relative phase retardation between the interfering beams, as instance, different geometries in the tiling of the dielectric medium are achievable [38]. By using direct writing techniques like the electron-beam lithography or single laser beam lithography [39] the spatial tiling of the quasi-lattice can be determined point-by-point. In these cases, usually, the quasiperiodic tiling is previously calculated by geometric rules or inflation algorithms. In the case of the octagonal Ammann-Beenker tiling [40] the unit cells consist of "squares" and "rhombuses" of equal side length. Analogously, the Penrose aperiodic tiling may be realized with several approaches. We consider not the original Penrose pentagonal tiling but the equivalent tiling of the plane generated with two "rhombuses" of different size. Both resulting quasicrystals have 5-fold rotational and mirror symmetry corresponding to a decagonal (10-fold) point group symmetry. Hence, we will refer to the Penrose "rhombus" pattern as decagonal. With regard to the PhQC of 12-fold rotational symmetry, we consider a dodecagonal tiling consisting of "squares" and "triangles" given by Stampfli inflation rule [41]. Although the rotational symmetry of the structure can remain unchanged, the quasiperiodic lattice can be completely different depending both on the particular tiling of the plane

used for the structure calculation and the particular experimental parameters adopted in the fabrication process as in the case of the multiple-beam holography.

For each symmetry, the two structures were calculated a) using a geometric or inflation rule, and b) supposing a multiple-beam interference process. Let us call geometric pattern the first and indicate it by the letter (A), and interferential the latter, indicated by the letter (B). The two patterns are analyzed and compared to provide a comprehension of the behaviour of the photonic band-gap with respect to the building tile for increasing order of symmetry and as a function of the refractive index difference $\Delta n$, in order to investigate the relationship between theoretical tiling and experimental tiling resulting from holographic fabrication processes.

The 8-fold geometric structure here studied was supposed made of dielectric rods (high index $n_H$ medium) in air (low index $n_L$ medium) located at the vertices of the Ammann-Beenker tiling of space, that is the positions of the cylinders of radius **r** are coincident with the vertices of "squares" and "45° rhombuses" with sides of equal length **a**. This structure is shown in Fig. 1-a. Recently, it was found theoretically that this quasiperiodic pattern presents a complete PBG with a very low threshold value for the refractive index difference, that is $\Delta n = n_H - n_L = 0.26$[19]. Moreover, the ratio $\Delta\lambda/\lambda_m$ between the gap width $\Delta\lambda$ and the midgap wavelength $\lambda_m$ is close to 5% for $\Delta n = 0.45$ with a typical attenuation of ~20dB, suggesting the possibility to realize optoelectronics devices based on the octagonal(A) tiling pattern in silica or even in soft materials like polymer. Holographic lithography permits to record large-area photonic quasicrystals in many kinds of photosensitive hard and soft materials, hence it represents an important fabrication technique largely employed to realize high quality quasiperiodic structures. The writing pattern of light is usually obtained as multiple-beam interference and, consequently, the

resulting spatial pattern of the dielectric modulation is different from the quasicrystal patterns achievable from inflation tiling. Therefore, the performance of this kind of experimental PQCs might be largely in disagreement with the expected estimation. In a typical experimental situation of N-beam interference [36], the irradiance profiles $I(\boldsymbol{r})$ achievable according to the relation

$$I(\mathbf{r}) = \sum_{m=1}^{N}\sum_{n=1}^{N} A_m A_n^* \exp[i(\mathbf{k}_m - \mathbf{k}_n)\cdot\mathbf{r} + i(\varphi_m - \varphi_n)], \qquad (2.22)$$

where $A_m$, $\mathbf{k}_m$, $\varphi_m$, are the amplitudes, the wave vectors and the initial phases of the interfering beams, respectively, give quasiperiodic spatial distributions of the intensity maxima.

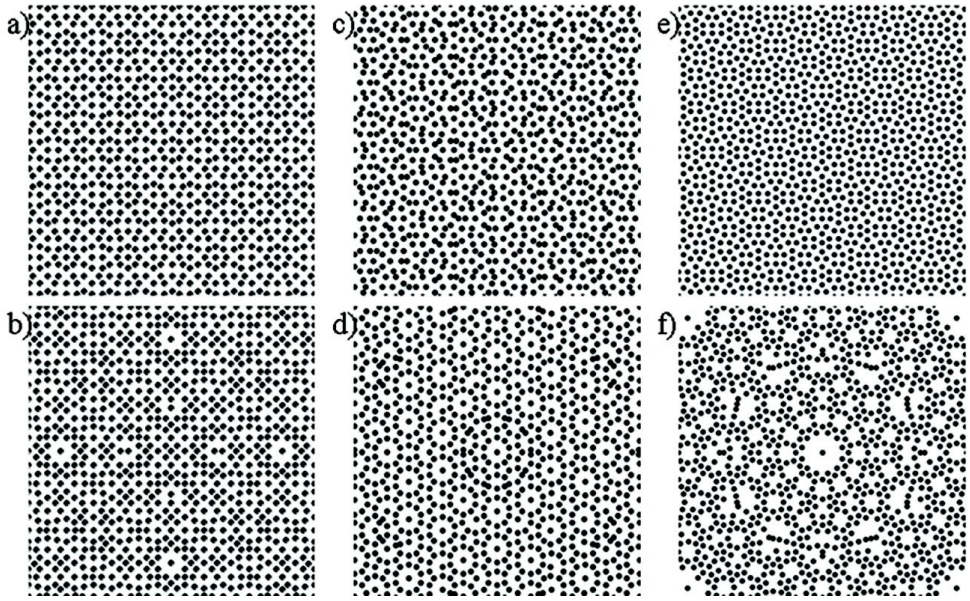


*Figure.2.1. (a)-(b) Octagonal quasiperiodic patterns of rods (top view) with geometric square-rhombus tiling (Ammann-Beenker) and interferential tiling, respectively; (c)-(d) decagonal patterns with geometric rhombic tiling (Penrose) and interferential tiling, respectively; (e)-(f) dodecagonal geometric triangle-square tiling (Stampfli inflation rule) and interferential tiling, respectively.*

Usually, the beams are supposed having the same linear polarization. Their number N is related to the rotational symmetry of the quasicrystal. By changing the phase retardation between the beams,

different patterns having the same symmetry can be realized. The filling factor, defined as the ratio between the area of $n_H$ regions and total area, depends on the threshold level of the photosensitive material and the exposure time and intensity. Typically, the maxima positions of the light pattern correspond to the high dielectric regions, that can be usually approximated with a structure of homogenous dielectric rods embedded in a host medium of different index. In Fig. 1-b, the 8-fold pattern is shown, calculated for N=8 from Eq. (2.22). The structure was obtained imposing a particular phase retardation between the beams, that is the phases were periodically shifted by $\pi/2$ so that $\varphi_1=\varphi_5=0$, $\varphi_2=\varphi_4=\varphi_6=\varphi_8=\pi/2$ and $\varphi_3=\varphi_7=\pi$. The pattern was obtained by positioning circular rods of radius $\boldsymbol{r}$ (top view in Fig. 1) in the maxima of the continuous irradiance distribution $\mathbf{I}(\boldsymbol{r})$ resulting from Eq. (2.22) [42]. The quasicrystal lattice is therefore determined without calculating a particular tiling of the plane. Nevertheless, the spatial tiling can be easily derived from the generated structure. The patterns depicted in Fig. 1-a and 1-b are clearly different. Although they possess the same rotational symmetry, the tiling originating the pattern provides a different assembly of the dielectric elements. The particular interferential pattern of Fig. 1-b, say octagonal(B), was studied in a preliminary work [42] promising to provide interesting PBG properties.

The patterns shown in Fig. 1-c and 1-d are 10-fold quasicrystals obtained from the geometric Penrose tiling with rhombic cells of equal side length and supposing 10-beam interference, respectively. Let us indicate the first as decagonal (A) and the latter as decagonal (B). The Penrose quasi-lattice represented in Fig. 1-c is an artificial PBG material that promises to find interesting application for optoelectronic and microwave devices [43]. In Fig. 1-e and 1-f, the dodecagonal(A) and dodecagonal(B) patterns obtained from inflation algorithm and 12-beam interference, respectively, are shown. In particular, dodecagonal(A) is a 12-fold quasicrystal formed with triangle-square

tiling by a recursive algorithm and scaled up by an inflation factor, that was found to induce a photonic bandgap even in host medium with low threshold index like glass ($\Delta n$=0.45) [4]. Both multiple-beam patterns of 10-fold and 12-fold symmetry have been calculated from Eq. (1) and (2) supposing a typical holographic process of fabrication in which the beams have the same linear polarization and equal optical phase, that is $\varphi_1$=...= $\varphi_8$=...= $\varphi_{12}$.

The two-dimensional Finite Difference Time Domain (FDTD) method with uniaxial perfectly matched layer (PML) boundary conditions was used in all simulations. The FDTD technique was employed to obtain transmission information, through the ($x$, $y$)-plane, as a function of propagation direction and wavelength, for both polarization TE (electric field $E_z$ perpendicular to the lattice plane) and TM (magnetic field $H_z$ perpendicular to the lattice plane). In each numerical calculation a Gaussian time-pulse excitation was simulated outside the structure or inside it for comparison. Several detectors (time monitors) were placed in particular positions allowing to store the field components. Their positions were chosen to cover the angular range related to the 8-, 10- and 12-fold rotational symmetry with an angular separation from 5° to 15° in relation to the structure studied. The Fourier Transform (FT) of the time-dependent signal collected by the detector provided the frequency response of the structure with high resolution. The corresponding transmission spectra had a wavelength range between 0.1 and 6.0$\mu$m with a resolution of $\delta$=5.0×10$^{-4}$$\mu$m, whereas the discretization grid provided a minimum of 100 grid points per free space wavelength. The transmission coefficient was calculated as a function of the refractive index difference $\Delta n$, for both TE and TM polarizations, for each propagation direction of the time-pulse source corresponding to a particular detector position. Fig. 1 shows a detail of the patterns that were analyzed in which the number of dielectric elements was held fixed to 900. Due to the non-geometric building of

the patterns depicted in Fig. 1-b, 1-d and 1-f, we found useful to define a new parameter, that is the average distance ***a*** between neighbouring rods along the x-direction, as characteristic length of the patterns. The filling factor can be related to the filling fraction r/a, that is the ratio between the rod radius r and the average distance a. Such parameter was held fixed to r/a=0.18 in each simulation to permit the comparison between the structures analyzed here.

## 4.2. Transmission properties of quasicrystal structures

As aforementioned, two different tiling patterns, obtained from geometric tiling and interference-based method, respectively, were analyzed for octagonal, decagonal and dodecagonal symmetry. In Fig. 2, the transmittance spectra related to the octagonal(A) (left panel) and octagonal(B) (right panel) patterns, obtained for increasing values of the refractive index difference Δn, in particular 0.4 (a)-(b), 0.6 (c)-(d) and 0.8 (e)-(f), are shown as a function of normalized wavelength λ/a, for both TE (black curve) and TM (red curve) polarizations. In the case of the octagonal (A) tiling, the bandgap starts to form even at $\Delta n$=0.4 (see Fig. 2-a), but only for TE polarization. As the dielectric contrast increases, the attenuation of the transmission signal in the bandgap region enhances from ~13dB to ~30dB (see Fig. 2-a and 2-e) with an increase of the width to midgap ratio $\Delta\lambda/\lambda_m$ from 2.4% at $\Delta n$=0.4 to 14.4% at $\Delta n$ =0.8. The attenuation was estimated by averaging the values obtained in correspondence of the spectral gap. The shift in the position of the bandgap, evident from the variation of the normalized midgap wavelength $\lambda_m$ /a from 1.22 to 1.38, is reasonable because increasing values of $\Delta n$ correspond to an increase in the average refractive index of the quasicrystal medium. In the case of the octagonal (B) tiling, the bandgap starts to appear at $\Delta n$ =0.6, centered at $\lambda_m$ /a =1.79, only for TE polarization also for this pattern (Fig. 2-d). In Fig. 2-f, two bandgaps are instead visible corresponding to $\Delta n$ =0.8.

One is centered at the normalized wavelength $\lambda_m$ /a =1.61 and the other one at $\lambda_m$ /a =1.93. The first bandgap has $\Delta\lambda/\lambda_m$ ~5% and presents a substructure of peaks possibly due to the existence of localized states.

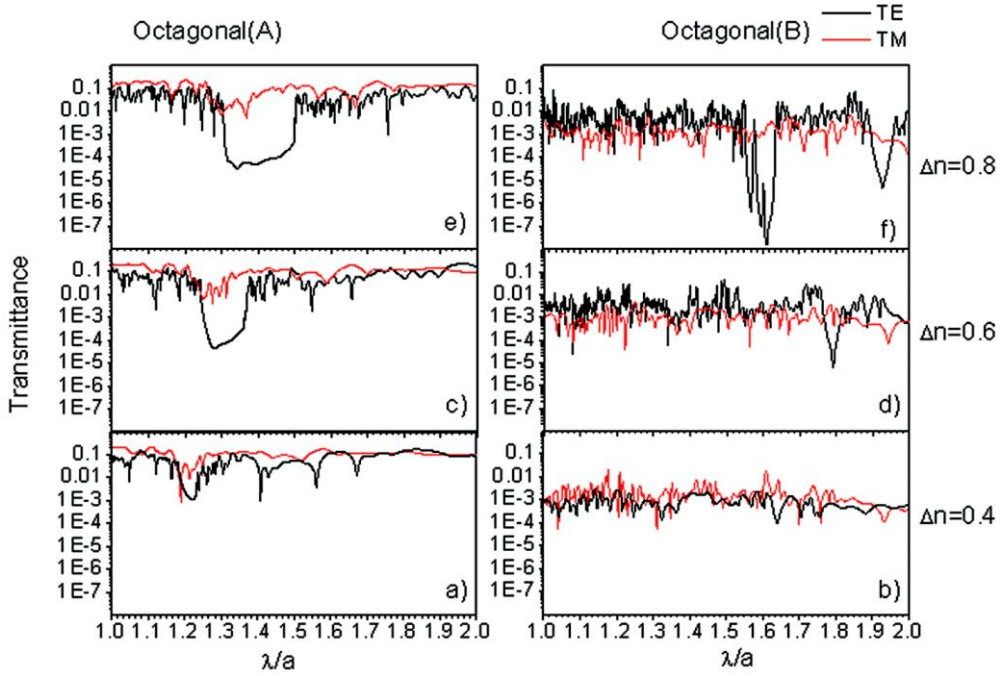


***Figure.2.2.*** *Transmittance spectra calculated for 8-fold symmetric structures with geometric tiling, say octagonal(A) (left panel), and interferential tiling, say octagonal(B) (right panel), for TE (black curves) and TM (red curves) polarizations, for increasing values of the refractive index difference: Δn=0.4 (a)-(b), Δn=0.6 (c)-(d), Δn=0.8 (e)-(f).*

Very interesting is the presence of strong transmittance attenuations, of the order of ~50dB and ~30dB, found in the gap regions at $\lambda_m$ /a =1.61 and $\lambda_m$ /a =1.93, respectively, both at $\Delta n$ =0.8 as evident in Fig. 2-f. From these first estimations, the differences arisen from the transmittance spectra clearly prove the importance of the tiling geometry in determining the photonic bandgap properties of the quasicrystal, independently from the dielectric contrast.

The quasicrystalline structures decagonal (A) and decagonal (B) were derived, as above discussed, from the well-known Penrose "rhombus" tiling and by simulating a 10-beam interference process, respectively. Analogous to the transmittance information reported in Fig. 2 related to the octagonal patterns, the corresponding TE (black line) and TM

(red line) transmittance spectra for both decagonal (A) (left panel) and decagonal(B) (right panel) patterns, obtained for $\Delta n$ =0.4 (a)-(b), 0.6 (c)-(d) and 0.8 (e)-(f), are shown as a function of normalized wavelength $\lambda/a$ in Fig. 3. For TE polarization, the decagonal (A) pattern shows a band gap at a refractive index difference $\Delta n$ =0.4 with a ~5dB attenuation (see Fig. 3-a), that enhances to ~20dB as the index difference increases to $\Delta n$ =0.6, with $\Delta\lambda/\lambda_m$ =3.7% at $\lambda_m$ /a =1.45 (see Fig. 3-c). The signal attenuation further increases to ~30dB with a normalized width $\Delta\lambda/\lambda_m$ =9% at $\lambda_m$ /a=1.5 for refractive index difference $\Delta n$ =0.8, as reported in Fig. 3-e. No clear PBG was found for TM polarization, at least for the values of dielectric contrast here examined. As evident from the right panel of Fig. 3, the decagonal(B) pattern, on the other hand, does not show any clear bandgap for TM polarization at $\Delta n$ =0.4 and 0.6, presenting only a narrow PBG with a ~10dB attenuation at $\Delta n$ =0.8. Moreover, the dodecagonal (B) tiling does not produce any remarkable bandgap for refractive differences lower than 0.8 also for TE polarization (see Fig. 3-b and 3-d). As shown in Fig. 3-f, a ~20dB attenuation is visible for TE polarization at $\Delta n$ =0.8 in a narrow spectral range in which many further peaks, associable to defect states, are present.

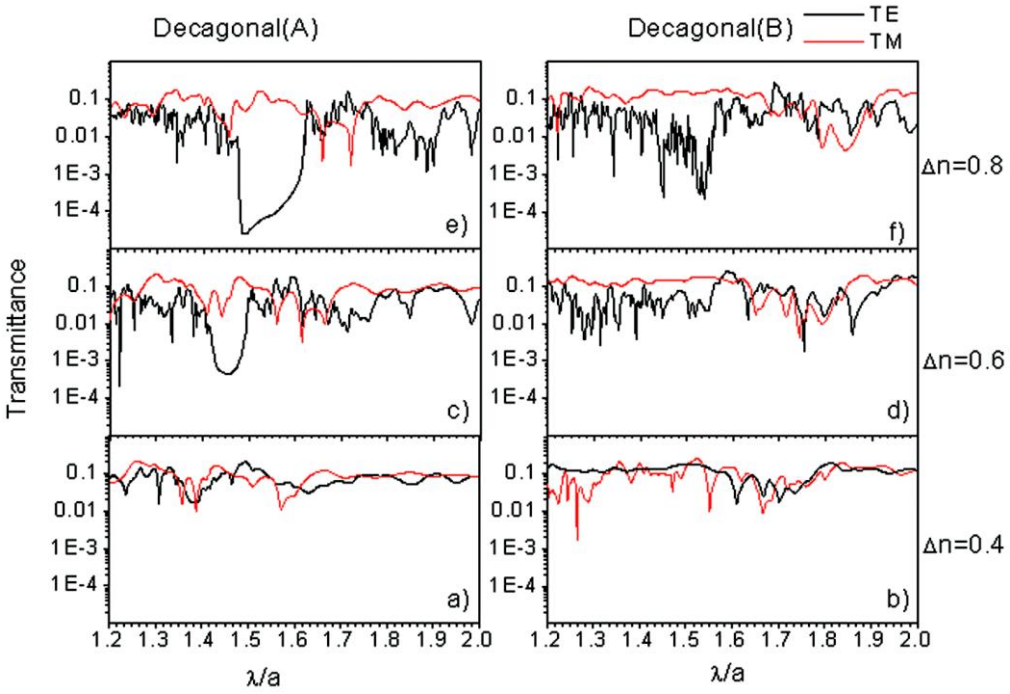


**Figure.2.3.** Transmittance spectra calculated for 10-fold symmetric structures with geometric tiling, say decagonal(A) (left panel), and interferential tiling, say decagonal(B) (right panel), for TE (black curves) and TM (red curves) polarizations, for increasing values of the refractive index difference: $\Delta n$=0.4 (a)-(b), $\Delta n$=0.6 (c)-(d), $\Delta n$=0.8 (e)-(f).

The transmittance spectra associated to the 12-fold quasicrystals, say dodecagonal (A) and (B), were finally calculated and reported for comparison in the left and right panels, respectively, of Fig. 4, analogously to the other quasicrystalline structures previously analyzed. For the dodecagonal (A) tiling pattern, the band gap starts to open up at $\Delta n$ =0.4 (Fig. 4-a), for TE polarization, becoming wider at $\Delta n$ =0.6 with a normalized width $\Delta\lambda/\lambda_m$ = 5.7% at $\lambda_m$ /a=1.24 and a ~25dB of attenuation in the transmittance coefficient (see Fig. 4-c). The band gap is shifted to $\lambda_m$ /a=1.34 with an increased width of $\Delta\lambda/\lambda_m$ = 10.3% and an attenuation of ~30dB at $\Delta n$ =0.8 (see Fig. 4-e). No remarkable photonic band gap is observed for TM polarization of the time-pulse excitation also in this case. The interferential pattern, or dodecagonal (B), shows only a very narrow band gap, for TE polarization, for an index difference as low as $\Delta n$ =0.6 in correspondence of the normalized

mid-gap wavelength $\lambda_m$ /a=1.42. The band gap width increases to $\Delta\lambda/\lambda_m$ =4.5%, slightly shifted to $\lambda_m$ /a=1.49, at $\Delta n$ =0.6 and with an attenuation <20dB, although few localized states are visible within this spectral region, as reported in Fig. 4-f. Also for the 12-fold symmetry, the patterns achievable from a geometric algorithm and resulting from a multiple-beam holographic process provide remarkable differences not only with regard to the PBG properties but also in relation to the existence of the band gap. Therefore, it is worth noticing how the tiling geometry affects the transmittance information independently from the dielectric contrast and the rotational symmetry of the quasi-lattices mentioned above.

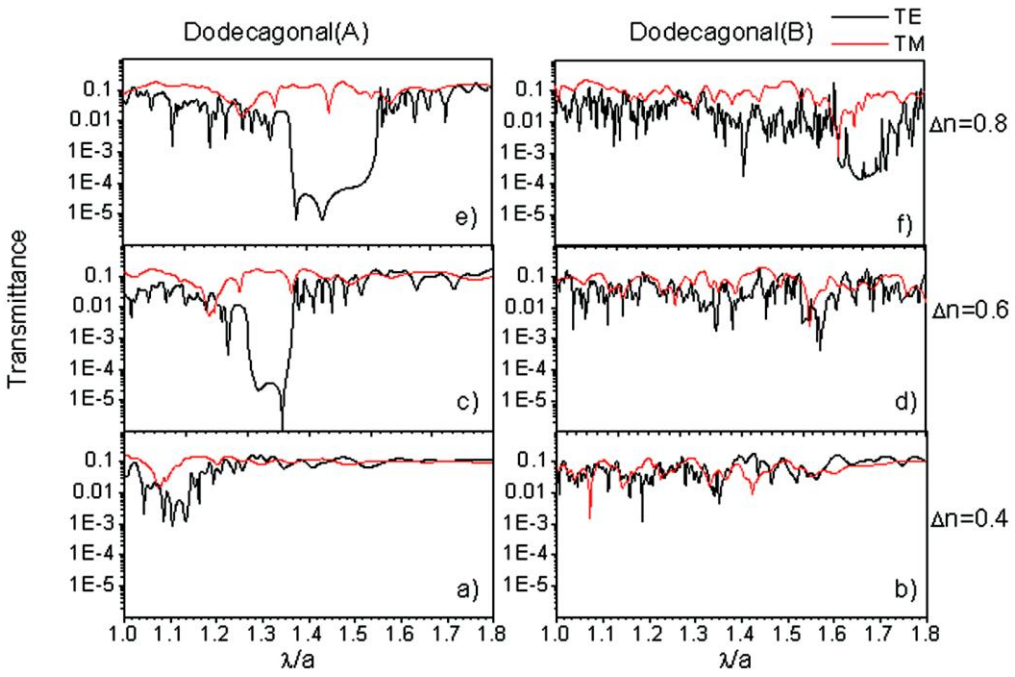


*Figure.2.4. Transmittance spectra calculated for 12-fold symmetric structures with geometric tiling, say dodecagonal(A) (left panel), and interferential tiling, say dodecagonal(B) (right panel), for TE (black curves) and TM (red curves) polarizations, for increasing values of the refractive index difference: Δn=0.4 (a)-(b), Δn=0.6 (c)-(d), Δn=0.8 (e)-(f).*

The numerical simulations of the transmittance spectra, based on the finite difference method, prove that, although the structures have the same symmetry, the different tiling geometry affects dramatically the

existence and behaviour of the photonic band gap. The patterns that we examined were chosen to highlight the substantial and remarkable PBG differences that arise between a quasicrystalline geometric tiling and a similar quasicrystal achievable from holographic fabrication techniques. Holographic lithography represents, in fact, an efficient and feasible fabrication method able to provide large-area photonic quasicrystals of high quality both in soft and hard materials. If wide PBGs are to be obtained at low index contrast, hence, very accurate control of the fabrication parameters is mandatory. In this direction, we recently have developed a single-beam holographic technique able to provide the desired tiling patterns in order to realize high efficiency PBG structures for photonic applications.

# Chapter 3

# Experiments in Microwave frequencies

This chapter is dedicated to the measurements done in microwave frequencies. The realization of the quasicrystal geometries functioning in the microwave frequencies is easier when compared to the nano-fabrication techniques required for optical quasicrystals. The experiments were carried out to study the band gap properties and field localization in photonics quasicrystals. Before going into the details of the experiments, the basic instruments and measurement techniques used in these experiments are briefly described.

## 1. Microwave measurement instruments

### 1.1. Vector Network analyzer (VNA)

This is the instrument used to generate and receive the radiation at microwave frequencies. A VNA measures the incident, reflected and transmitted radiation that travel along the transmission lines. The basic architecture of a vector network analyzer include a generator, a test set which includes two ports, a control panel and RF cables to connect the device under test (DUT).

In order to understand how the microwave signals are modified as they travel along a microwave photonic two port, the scattering parameter (S-parameter) approach can be used as shown in the fig (3.1). The defining equations are:

$$\begin{bmatrix} b_1 \\ b_2 \end{bmatrix} = \begin{bmatrix} S_{11} & S_{12} \\ S_{21} & S_{22} \end{bmatrix} \begin{bmatrix} a_1 \\ a_2 \end{bmatrix}$$

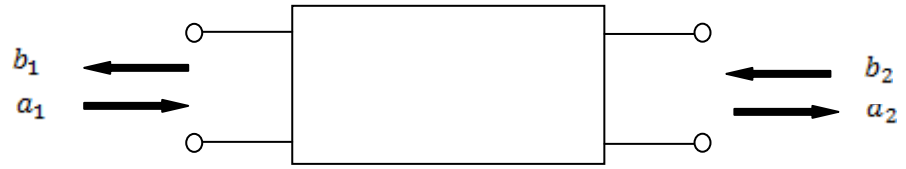


*Figure.3.1. Representative diagram of a two-port device*

The individual S-parameters are as the following:

$S_{11} = \left.\frac{b_1}{a_1}\right|_{a_2=0}$ = input reflection coefficient ( with output port matched).

$S_{21} = \left.\frac{b_2}{a_1}\right|_{a_2=0}$ = forward transmission coefficient (withoutput port matched).

$S_{12} = \left.\frac{b_1}{a_2}\right|_{a_1=0}$ = reverse transmission coefficient ( the input port matched).

$S_{22} = \left.\frac{b_2}{a_2}\right|_{a_1=0}$ = output reflection coefficient ( the input port matched).

Here $a_n$ and $b_n$ represent the incident and reflected travelling power at port $n$. They are related to the incident and reflected current and voltages.

$$a_n = \frac{V_{ni}}{\sqrt{Z_{0n}}} = I_{ni}\sqrt{Z_{0n}}$$

$$b_n = \frac{V_{nr}}{\sqrt{Z_{0n}}} = -I_{nr}\sqrt{Z_{0n}}$$

where $V_{ni}$ and $V_{nr}$ are the incident and reflected voltages at port $n$, $I_{ni}$ and $I_{nr}$ are the incident and reflected currents at port $n$, respectively. Matching of the impedances is achieved by using the terminating impedances equal to the characteristics impedance $Z_{0n}$. In the case of microwave S-parameters, the characteristics impedance is 50Ω. The VNA measures these scattering parameters from which the reflectance or transmittance properties of the DUT can be obtained.

Before starting any measurements, it is necessary to calibrate the VNA in order to get accurate measurements. There are several procedures for calibrating a VNA. Depending on the measurement to be done, the method for calibration can be determined. Each network analyzer can be separated into an error network and an ideal network analyzer. After calibration, the analyzer computes the error terms using the values it measured during the calibration process along with the characteristic data of the standards. It is then possible to correct the raw measured values in later measurements and calculate S-parameters for the device under test.

## 1.2. Microwave Antennas

Different kinds of antennas are used to radiate and receive the microwave radiation. The most important features of an antenna is the directivity and impedance match. An antenna should be able to couple or radiate the energy effectively into air. So an antenna should have an impedance matching with that of the air. It is necessary to maintain the impedance match between the system and the antennas throughout the measurements and for the frequency range used. The directivity of the antenna refers to the narrowness of the radiation pattern of the antenna. The power gain of the antenna increases as the degree of directivity increases. In the experiments described in the following sections, two different antenna configurations are used depending on the measurement technique.

In the case of free space measurement, horn antennas were used as transmitter and receiver. The shape of the radiation pattern of a horn antenna depends on the shape of the horn. The ratio of the horn length to the size of its mouth determines the beam angle and directivity. In general, the larger the mouth of the horn, the more directive is the field pattern. In the case of parallel-plate experiments, the coaxial line terminations were used as monopole radiators.

# 2. Experiments in the microwave frequencies

## 2.1. Band gap properties of low-index contrast photonic quasicrystals

As described in the chapter 1, photonic quasicrystals have several peculiar properties which make them suitable candidates for many photonic applications. In this section, some very interesting properties of the band gap formed by some of the quasiperiodic geometries are discussed. Special attention has been given to structures with lower refractive index contrasts taking into account of their usefulness in fabrication techniques using holographic lithography. A detailed numerical study on this kind of structures with low index contrasts was presented in the previous chapter.

Another critical parameter that comes into play for the realization of devices such as light emitting diodes is the isotropy of the photonic band-gap. The periodic structures with square or triangular lattices have anisotropic band-gap properties because of the anisotropy of Brillouin zone. Because of their non-conventional higher order rotational symmetry, PQCs may possess highly isotropic band-gaps instead. Experimental investigations in this direction was performed by Bayindir *et al.*[22] in the microwave regime and by Hase *et al.*[23] in the far infrared region, based on octagonal and Penrose quasicrystals. Both studies reported the appearance of a photonic band gap having almost isotropic properties in aperiodic lattices consisting of dielectric rods in air and for electric field parallel to the rods.

The aim of this work is to have a detailed and systematic analysis of the band-gap isotropy of photonic crystal and quasi-crystal structures having low refractive index contrast and for both TE and TM field polarization. Different geometries are studied to have a comparative analysis. The geometries investigated are the following: periodic hexagonal pattern with 6-fold symmetry (Fig 1(a)), and quasicrystals

geometries with 12-fold symmetry (dodecagonal), 8-fold symmetry (octagonal) and 10-fold symmetry (Penrose decagonal) as shown in Figures1 (b), (c) and (d) respectively. The PBG properties are studied both numerically and experimentally for two different index-contrasts: 0.60 and 0.44. The index contrast is defined here simply as the difference between the refractive index of the dielectric material and air.

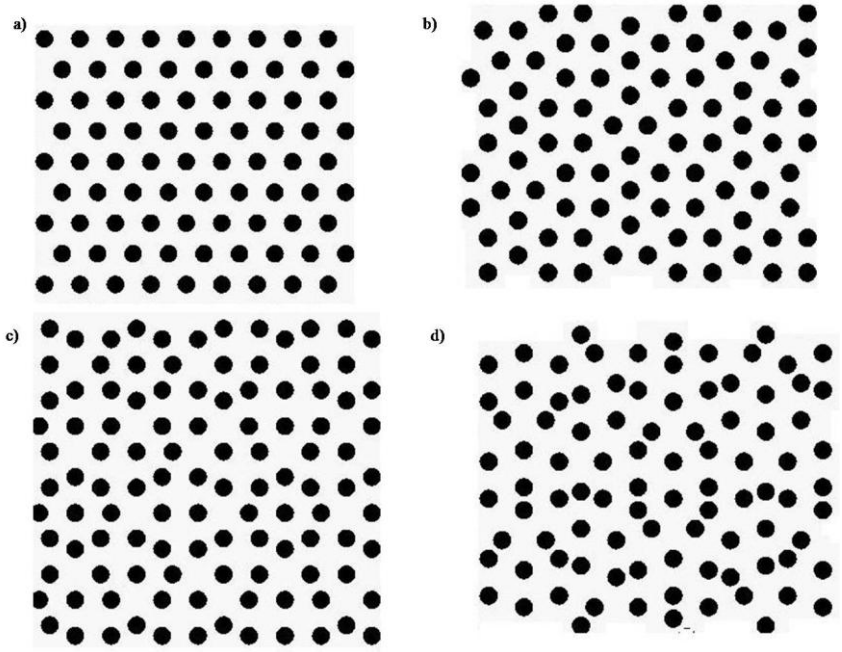


***Figure.3.2. The periodic and aperiodic geometries under study: (a) hexagonal, (b) dodecagonal, (c) octagonal, and (d) decagonal (Penrose).***

### 2.1.1. Computational and experimental methods

The photonic crystals studied consist of dielectric cylindrical rods in air placed on the vertices of tiles in the corresponding geometry. The filling factor is set to be the same for all the structures under study, and is equal to 0.23. The geometries used are shown in Figure1. They are designed to have approximately 400 rods in an area of 40 cm x 14 cm. From the computational point of view, each quasicrystal structure

presents a challenge in obtaining the information about the photonic band-gap since the Bloch theorem cannot be applied in the calculations because of the lack of translational symmetry. The Finite Difference Time Domain (FDTD) technique is useful in this respect. FDTD method with uniaxial perfectly matched layer (PML) boundary conditions is employed to obtain transmission characteristics as a function of frequency of the incident radiation, propagation direction and polarization. In each simulation, the source of excitation is placed outside the crystal structure and the field components after propagation through the crystal are collected using a detector placed on the other side of the crystal. The Fourier transform of this data gives the transmission properties as a function of wavelength. In order to understand the isotropic properties of the photonic band-gaps, the spectra are obtained by varying the angle of incidence for all the structures. Both TE and TM polarizations were analyzed in the simulations.

The experiment was designed to be carried out in the microwave frequencies (8-20 GHz). Rexolite and Teflon having radius 0.64 cm and length 60 cm were used to build up the structures. These materials show a dielectric constant of 2.56 and 2.1 respectively in the frequency region of interest and a relatively low dissipation. Loss tangent values for Rexolite and Teflon are in the range of $10^{-4}$. In order to build up the structure, circular holes with the designed geometries have been drilled onto two support plates made of very low-refractive index material. Then, they are fixed 60 cm apart to be filled with the rods. In order to obtain the transmission characteristics of the crystals, two horn antennas acting as transmitter and receiver and connected to a two-port vectorial network analyzer (VNA) HP 8720C have been used. Before each measurement, the horn antennas are positioned and adjusted in order to have maximum transmission and the VNA is calibrated. Then the transmission curve is obtained by introducing the

crystal in between the two horn antennas. In order to measure the transmission as a function of direction of propagation of the incident radiation, the crystal is rotated through 5°, 10°, 15°, 20°, 25° and 30° in respect to the normal direction while keeping the position of the antennas unchanged. Measurements were also carried out as a function of crystal thickness, for normal transmission only. To change the field polarization, both horn antennas are rotated by 90° before each set of measurements

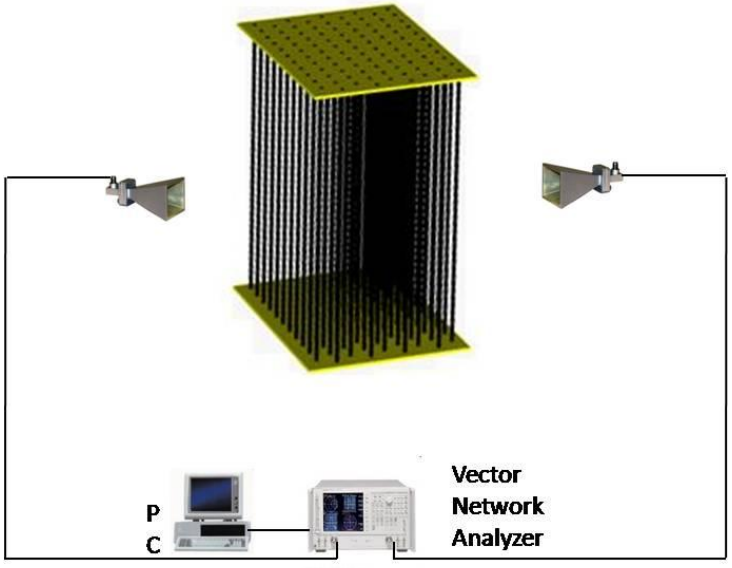


***Figure.3.3. Schematic diagram of the experimental set-up. Horn antennas are used to transmit and receive the microwave radiation. Data are collected using a vectorial network analyzer computer-controlled. The size of each structure (periodic or aperiodic) is 40×14×60 cm³.***

### 2.1.2 Results and discussions

### 1/ Refractive index contrast 0.60

### a) TE polarization

In order to study the isotropic nature of the PBG, the transmission characteristics are obtained as a function of incidence angle for all geometries under study. Figure2 shows the experimental and calculated transmission spectra for the hexagonal photonic crystal with an index contrast of 0.60 for various angles of propagation as indicated

in the figure. The experimental results are presented in Fig.3.3(a) whereas Fig.3.3(b) shows the corresponding simulation data. From the graphs it is clearly observed that the transmission spectra change drastically as the angle of propagation is changed from 0° to 30°. In the case of normal signal incidence (0°), the region of low transmission (photonic band-gap) is centered at about 11 GHz and spans for ~ 2.6 GHz, with almost no change for an angle 10°. However, as the angle is increased to 20°, changes are clearly visible. The center of the PBG is shifted to 12 GHz whereas its width becomes larger (~ 3.3 GHz). For an angle of 30°, the widening of the PBG is even stronger.

The transmission characteristics of a dodecagonal PQC structure are shown in Figure3. The experimental (Fig.3.4 (a)) and simulation (Fig.3.4 (b)) results put in evidence in this case that the PBG is quite isotropic. The position and width of the PBG remains almost the same for all the angles considered. The numerical and experimental results for the case of the octagonal geometry are presented in Figures 3.5(a) and 3.5(b) respectively. Transmission spectra are only slightly affected by the change of the angle of propagation. The PBG is centered at 11.5 GHz for angles from 0° to 10° whereas it is shifted to ~11.8 GHz for incidence at larger angles. There is also a small variation in the width of the PBG, from 1.4 GHz to ~2 GHz.

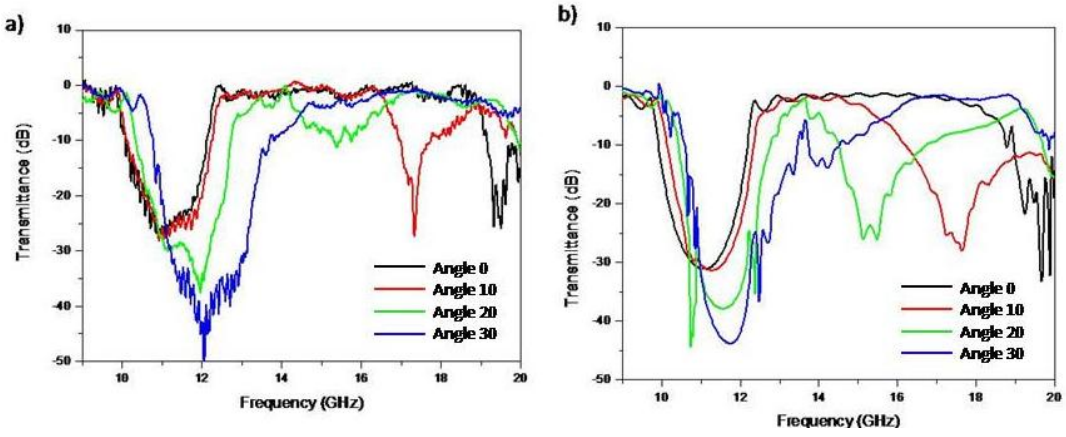


***Figure 3.4. (a) Experimental and (b) calculated transmission spectra of the hexagonal photonic crystal. Curves of different colours correspond to different angles of incidence as indicated in the graph.***

The results obtained for the Penrose tiled quasicrystal are shown in figures 3.6 (a) and 3.6(b). The bandgap is not as deep and wide as in the other cases. However, its angular dependence If the transmission at normal incidence (0°) is considered, the hexagonal crystal shows the widest PBG compared to all other structures under study. The PBG for the periodic crystal is around 2.6 GHz. In the case of aperiodic structures, this value decreases from 2.2 GHz (octagonal) to 2 GHz (dodecagonal) down to 1.1 GHz (Penrose).

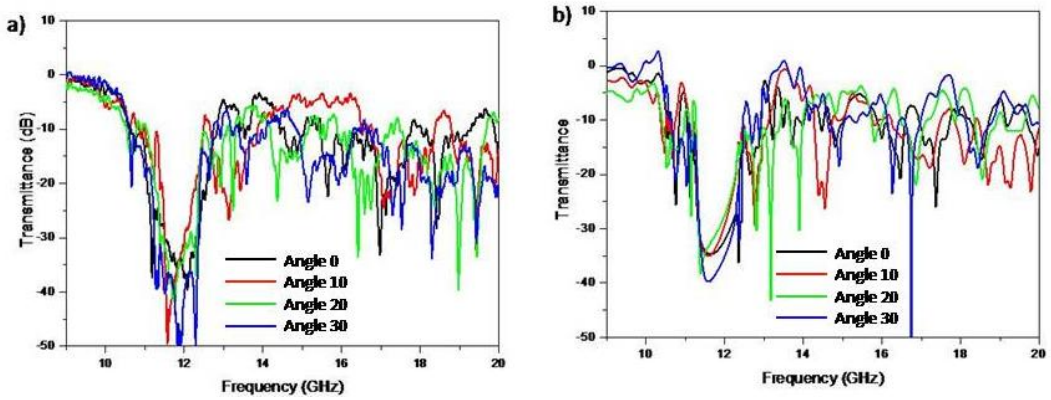


*Figure.3.5. (a) Experimental and (b) calculated transmission spectra of the dodecagonal photonic crystal. Curves of different colours correspond to different angles of incidence as indicated in the graph.*

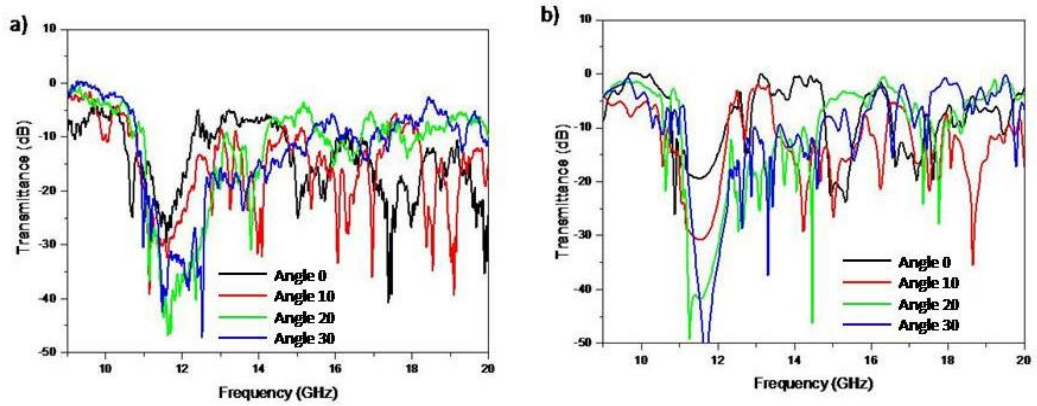


*Figure.3.6. (a) Experimental and (b) calculated transmission spectra of the octagonal photonic crystal. Curves of different colours correspond to different angles of incidence as indicated in the graph.*

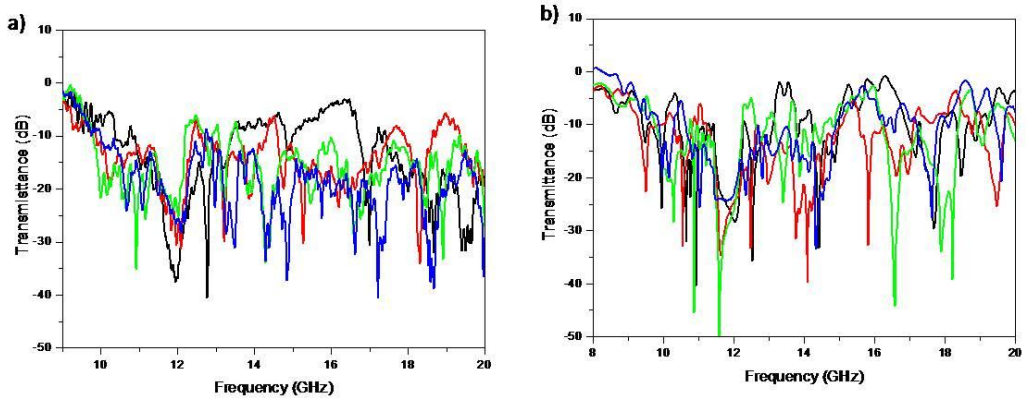


***Figure.3.7. (a) Experimental and (b) calculated transmission spectra of the Penrose photonic crystal. Curves of different colours correspond to different angles of incidence as indicated in the graph.***

In order to better understand the directional variation of PBG, we measured the upper and lower PBG boundaries as a function of the propagation angle. The band gap edges are defined as the frequency values for which attenuation reaches 15 dB. The hexagonal geometry clearly shows a strong dependence of the upper and lower frequency edges as a function of angle, whereas the PBG width seems to be less affected, as shown in Figure 3.7(a). The results for the dodecagonal structure, instead, clearly indicate (see Figure 3.7(b)) that its response is highly isotropic, with very small variations of the PBG width and edges at different angles from 0° to 30°. The properties for the octagonal geometry lie somehow in between, since it shows less isotropy compared to the dodecagonal geometry and noticeable width dependence in respect with the hexagonal case as displayed in Figure 3.7(c). Penrose geometry also seems to have quite isotropic, but narrower PBG (Figure 3.7 (d)).

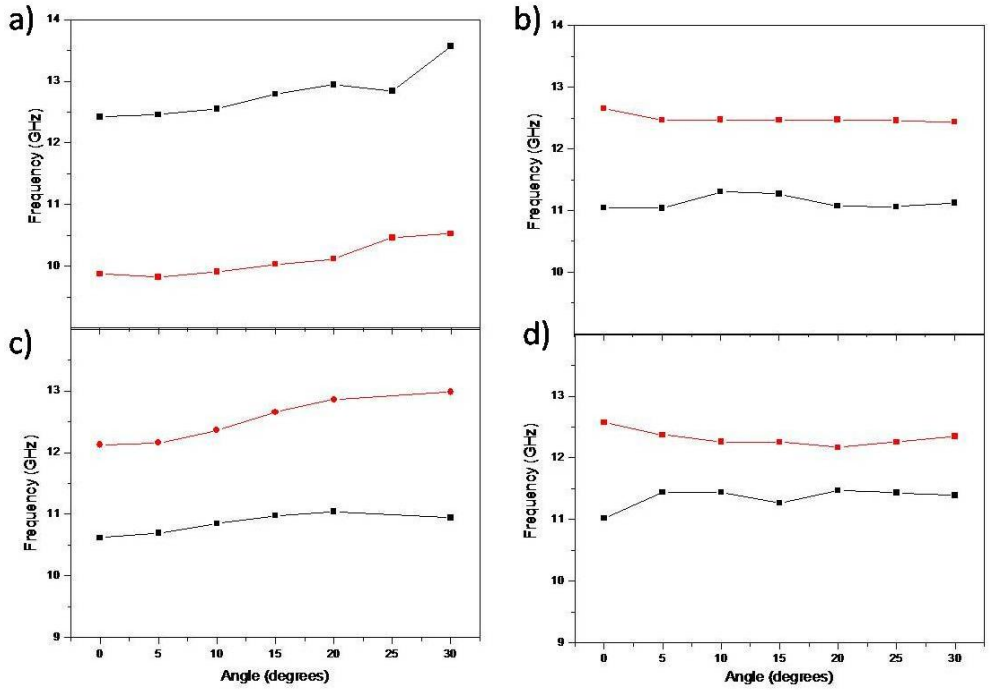


***Figure.3.8. Variation of PBG as a function of angle for the different geometries: (a) hexagonal, (b) dodecagonal, (c) octagonal and (d) Penrose. In each graph, the black and the red curves indicate the lower and upper frequency edges of the band gap respectively.***

### b) TM polarization

Simulation of the response to a TM polarized wave for all the geometries under study shows that for such low values (0.60 and 0.44) of the refractive index contrast the transmission characteristics of the Penrose and octagonal structures are nearly featureless. The results obtained for the hexagonal and dodecagonal geometries are shown in Figure8. The hexagonal geometry (Figure 3.8(a)) shows a clear PBG ~ 1.7 GHz wide and centered at about 11.7 GHz. The experimental (black curve) and calculated (red curve) results are in good agreement. The dodecagonal structure (Figure 3.8(b)) shows in the simulation spectra (red curve) two narrow dips in the transmission around 11.7 GHz and 13 GHz, which are however not well reproduced by the experimental data (black curve).

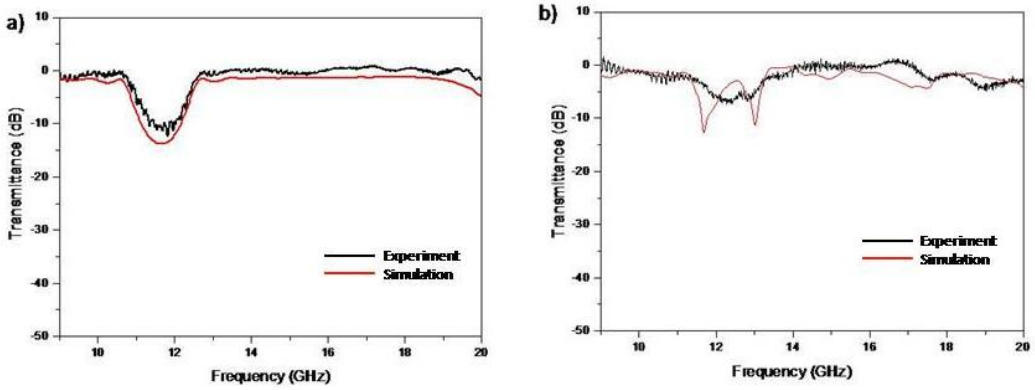


***Figure.3.9. The transmission curves for (a) hexagonal and (b) dodecagonal geometries for TM polarization. Both experimental and simulated results are shown in each graph.***

The results presented in this case are for TE polarization and the hexagonal and dodecagonal cases only. For TM polarization, no clear band-gap is formed in the geometries discussed as clearly observed from the simulations. The results are comparable with the case of the higher refractive index contrast presented above. The PBG is not as deep as in the case of Rexolite. In this case too, the hexagonal crystal shows a clear variation in the PBG properties as the angle of propagation is varied, as seen in the Figures 3.9(a) (experiment) and 3.9(b) (simulation). Similar results for the dodecagonal crystal are presented in Figure 3.10(a) and (b). The PBG frequency shift is less in comparison with the hexagonal crystal but the PBG is much narrower. A graph showing the variation of the upper and lower band-edge frequencies as a function of angle is also plotted in this case and shown in Figure 3.11.

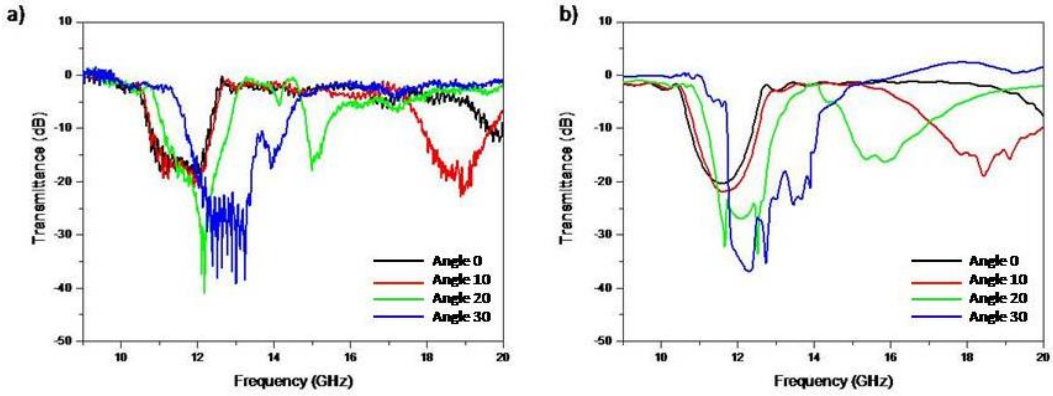


***Figure.3.10. (a) Experimental and (b) calculated transmission spectra of the hexagonal photonic crystal with an index contrast of 0.44. Curves of different colours correspond to different angles of incidence as indicated in the graph.***

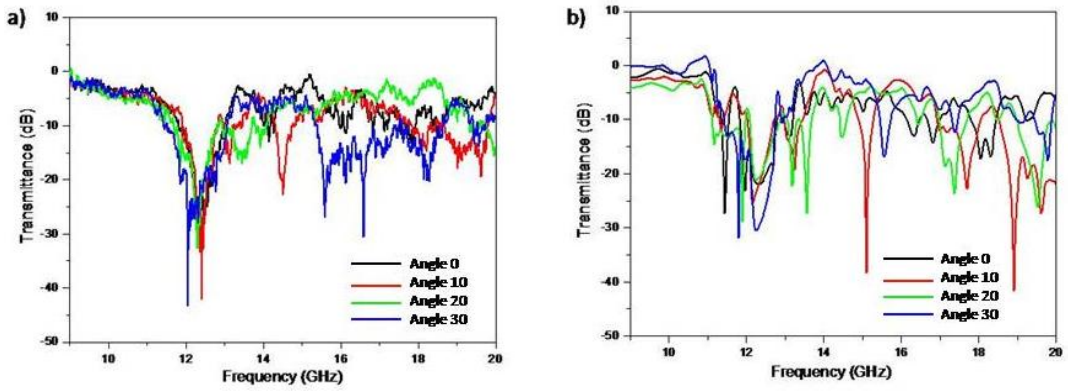


*Figure.3.11. (a) Experimental and (b) calculated transmission spectra of the dodecagonal photonic crystal with an index contrast of 0.44. Curves of different colours correspond to different angles of incidence as indicated in the graph.*

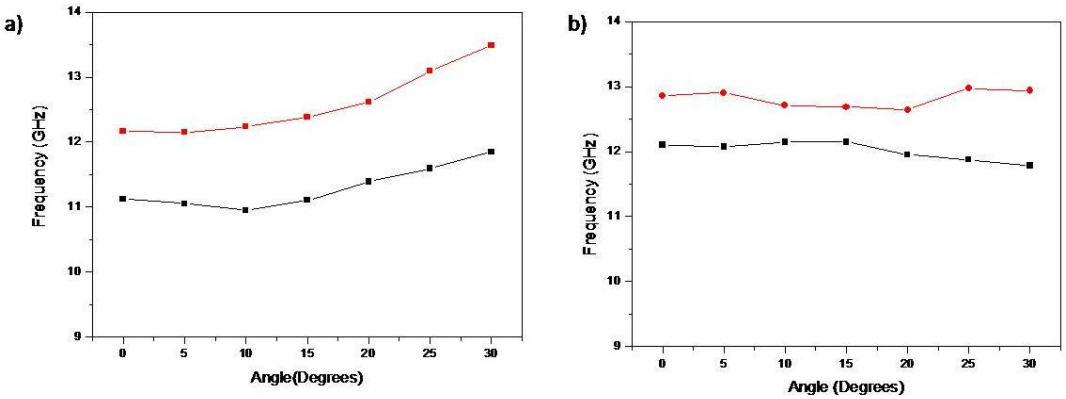


*Figure.3.12. Variation of PBG as a function of angle for (a) hexagonal and (b) dodecagonal geometries. In each graph, the black and the red curves indicate the lower and upper frequency edges of the band gap respectively.*

Although complete photonic band gaps cannot exist in low-index-contrast structures, it is shown that two-dimensional band gaps are possible for specifically polarized electromagnetic modes. Notably, gaps in quasicrystal geometries are more isotropic than those in crystals, due to their disallowed rotational symmetries. Even at very low dielectric contrast, the sixfold crystalline structure yields the greater bandgap than the quasicrystalline ones. For specific applications, however, very isotropic PBGs may be desirable, even if the size of the full gap is slightly reduced.

## 2.2. Observation of defect free localized state and waveguiding

Photonic quasi crystals (PQCs), like their periodic counter parts exhibit interesting electromagnetic properties such as, confinement and localization [44] of radiation etc. The electromagnetic response of a PQC can strongly depend on the short-range order of the lattice. Because of their structural peculiarities such as higher order of rotational symmetries (>6, which are not allowed for periodic crystals) and presence of many non –equivalent sites they show interesting properties like defect-free localized states [13].If in a periodic photonic crystal, localized modes are generated by intentionally creating defects, many PQCs show localized modes even without disturbing the geometry. These localized states are also found to affect the transmission of radiation within the waveguide in the vicinity of localization [13].

Some interesting transmission properties of a photonic quasicrystal made of cylindrical dielectric rods arranged in air according to a specific geometry with 8-fold rotational symmetry are presented in this section. The aim of this study is to analyze the possibility of manipulating the transmission properties of quasicrystals structures for possible photonic applications. We present the results to show some peculiar waveguiding properties of the particular geometry obtained from numerical full wave simulations and experimentally verified by measurements done in the microwave frequencies (7-11 GHz).

The quasicrystal geometry used in this experiment is chosen from one among the structures numerically studied in chapter 2. It is obtained by simulating the interference pattern of 8 beams according to the following formula:

$$I(\mathbf{r}) = \sum_{m=1}^{N}\sum_{n=1}^{N} A_m A_n^* \exp[i(\mathbf{k}_m - \mathbf{k}_n)\cdot\mathbf{r} + i(\varphi_m - \varphi_n)],$$

With N=8 and $A_m$, $k_m$,and $\varphi_m$ are the amplitudes, the wavevectors and the initial phases of the interfering beams, respectively. The dielectric cylinders are placed in the regions of maximum intensity. The phase of the interefering beams were periodically shifted by $\frac{\pi}{2}$ such that $\varphi_1 = \varphi_5 = 0,\ \varphi_2 = \varphi_4 = \varphi_6 = \varphi_8 = \frac{\pi}{2},\ \varphi_3 = \varphi_7 = \pi.$ The finite structure used in the studies is composed of cylindrical rods of alumina (dielectric constant ε=8.6) having radius of 0.3 cm and height 1cm (with a filling factor of 0.23). The rods are placed in air according to the 8-fold symmetrical pattern shown in figure (3.12).

The numerical simulations were performed using MEEP (MIT Electromagnetic Equation Propagation) which uses the finite difference time domain (FDTD) methods to analyze the electromagnetic transmission properties of the given structure. The 2D code assumes the dielectric rods to be infinitely long. All the analysis were done for the TE polarization of the electromagnetic waves. As a preliminary step we studied the transmission properties of the structure near the photonic band gap (PBG) region. This is done by illuminating the structure from outside using a pulsed source of electromagnetic radiation and collecting the transmitted radiation on the opposite side. As can be seen from fig (2.a), the photonic band-gap spans from around a/λ =0.25 to a/λ =0.35 GHz, which also includes a local high transmittance region around the normalized frequency (a/λ) 0.33. The field is localized within the defect-free structure when illuminated with radiation of normalized frequency 0.33 as shown in Fig (3.12).

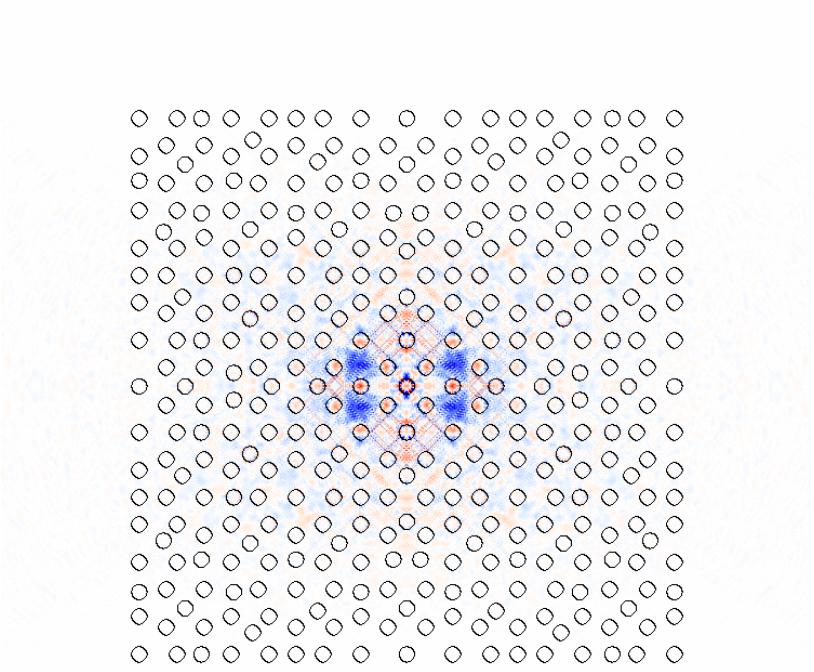

*Figure.3.13. The 8-fold symmetric pattern showing the field confinement*

Further analysis was done to study the wave guiding properties of the structure within the band-gap frequencies, especially near this localized state. A linear waveguide was created within the structure by removing three columns of rods from the middle. The electric field vector in the linear waveguide was mapped for CW radiation of different frequencies within the band-gap region. It is found that when the normalized frequency of the radiation is around the frequency corresponding to the localized state, the radiation is not guided after the center of the structure as seen from Fig (3.13). For all other frequencies, the radiation is guided through the PQC like in any other photonic crystal waveguide. To further understand the effect of the localized state in the transmission properties of the PQC, we studied the transmission of radiation within the waveguide when a dielectric pillar (with r=0.3cm and ε=8.6) is placed at the center of the structure. It is seen that EM radiation with frequencies corresponding to the the localized state are transmitted through the waveguide like all other frequencies as opposed to what happened in the waveguide without the central pillar (Fig 3.14). It is evident from Fig (3.15) that the presence

of localized state within the PBG is the reason for the reduced transmission at those frequencies within the waveguide. When the dielectric pillar is placed in the center of the waveguide, the field is no more localized which permits the radiation to escape through the waveguide.

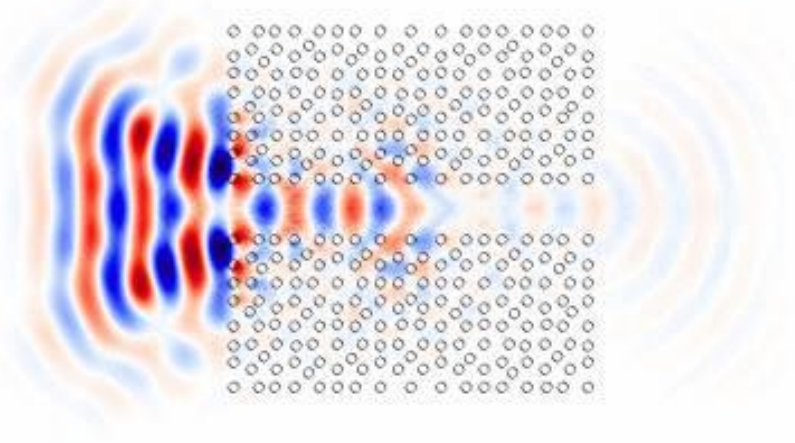

***Figure.3.14. The transmission at normalized frequency 0.33 (without the central pillar)***

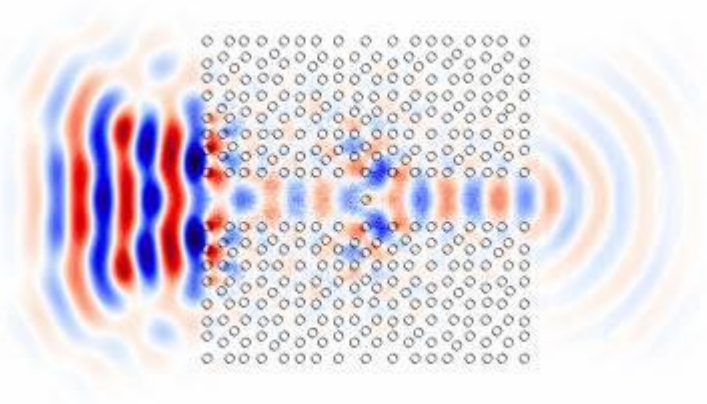

***Figure.3.15. The transmission at normalized frequency 0.33 (with the central pillar)***

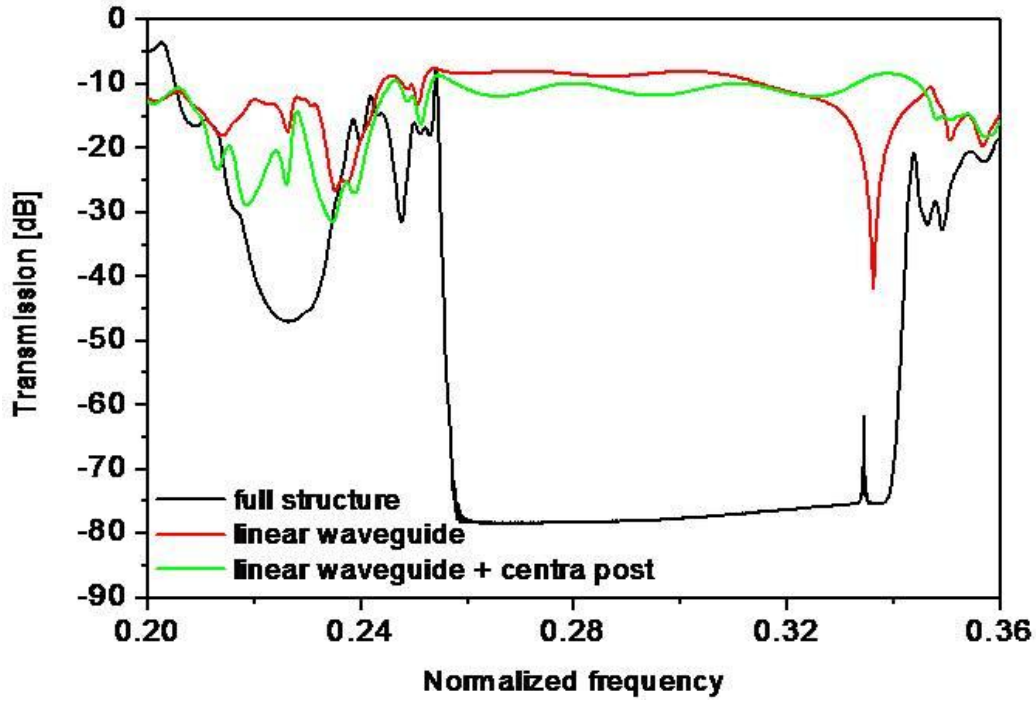


***Figure.3.16. Numerically simulated transmission characteristics of the structure. The black curve indicates the full structure while red and green shows the transmission characteristics of the structure with linear wave guide in the absence and presence of the central pillar respectively.***

In order to experimentally verify the results, we designed an experiment to be performed in the microwave frequencies. The geometry was realized by arranging alumina rods (h=1cm r=0.3cm ε=8.6) in air. An X-Y robot realized using stepper motor was used to arrange the rods in the exact position. The experiment was carried out in a parallel plate configuration. The transmission characteristics were measured using two monopole antennae connected to a vector network analyzer (VNA). Suitable absorbers were used in order to isolate the structure from any boundary effects.

Transmission characteristics around the PBG region were measured for of the geometry for the following conditions:

(1) The whole structure without any defect,

(2) The structure with the linear waveguide and

(3) For the structure with the pillar at the center of the linear waveguide.

The experimental results are in a very good agreement with the simulation results (Fig ). The mapping of the electric field within the waveguide is done for selected frequencies by moving one of the monopole antenna using the X-Y robot within the waveguide while the other antenna was kept fixed. The results for 10.06GHz are shown in Fig (TBD) which shows the difference in transmission of the radiation with and without the central dielectric pillar in the waveguide. The presence of the central pillar clearly improves the transmission of radiation with frequency corresponding to a localized state.

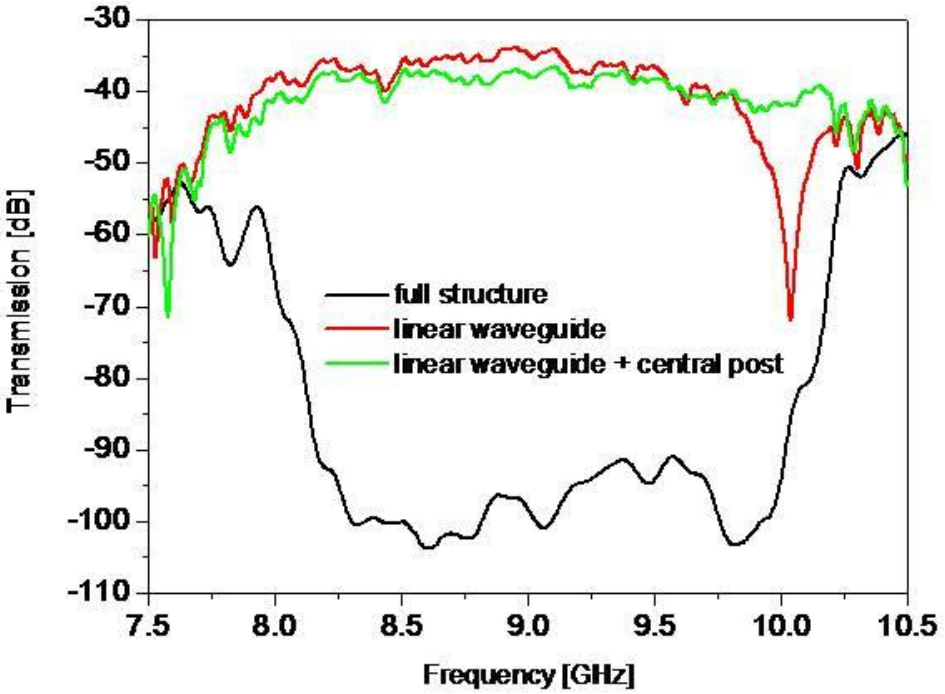


***Figure.3.17. Experimental transmission characteristics of the structure. The black curve indicates the full structure while red and green shows the transmission characteristics of the structure with linear wave guide in the absence and presence of the central pillar respectively.***

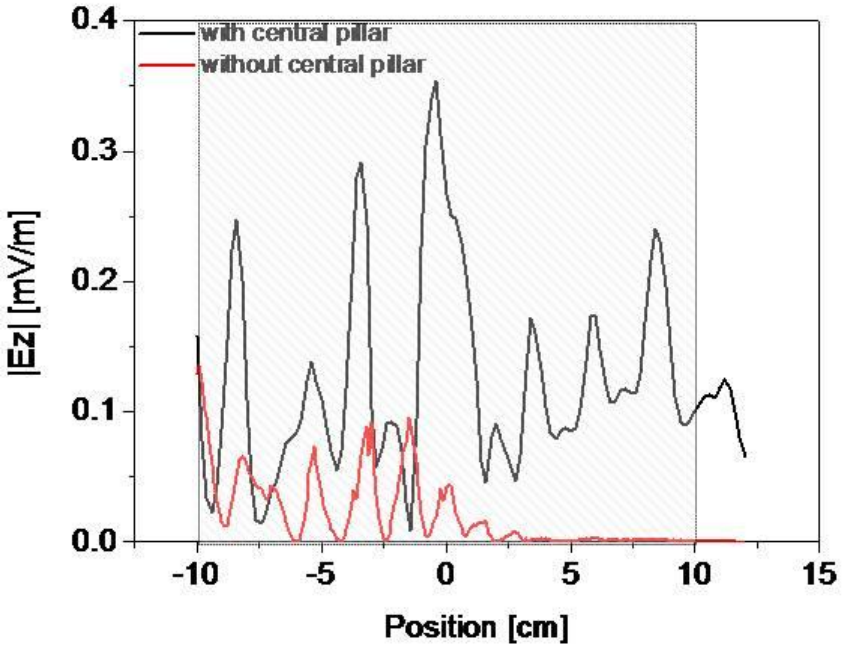


***Figure.3.18. Mapped electric field in the waveguide (black curve corresponds to the waveguide with the central pillar and the red curve corresponds to the wave guide without the pillar.)***

The effect of the properties of the central pillar to the localized state (and hence to the transmission of radiation) was also studied numerically. It is found that both the size (radius) and the dielectric constant of the central pillar within the waveguide will change the transmission properties. The numerical simulations shows that, as the dielectric constant of the pillar is increased, the localization of field is disturbed and shifted and almost completely disappears (Fig(3.18)). So the transmission characteristics can be tuned by changing the properties of the defect pillar. Almost similar tuning properties are shown by the change of radius of the central pillar by fixing the dielectric constant to $\varepsilon$=8.6 (Figure(3.19)).

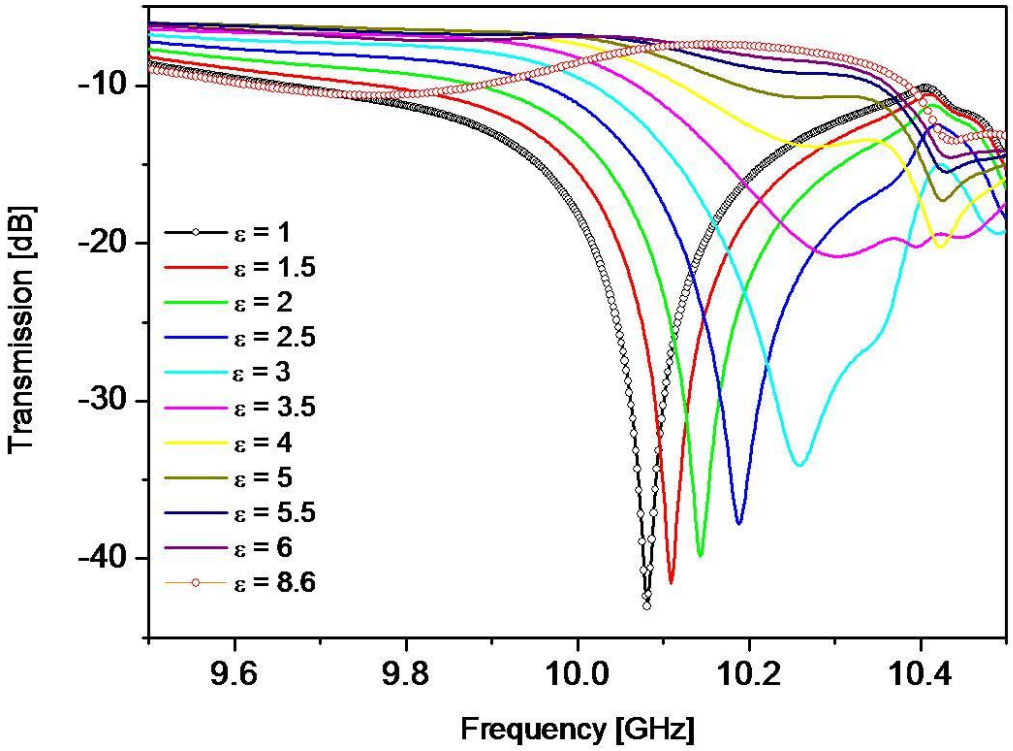


*Figure.3.19. Curves showing the dependence of the localized state on the dielectric constant of the central pillar*

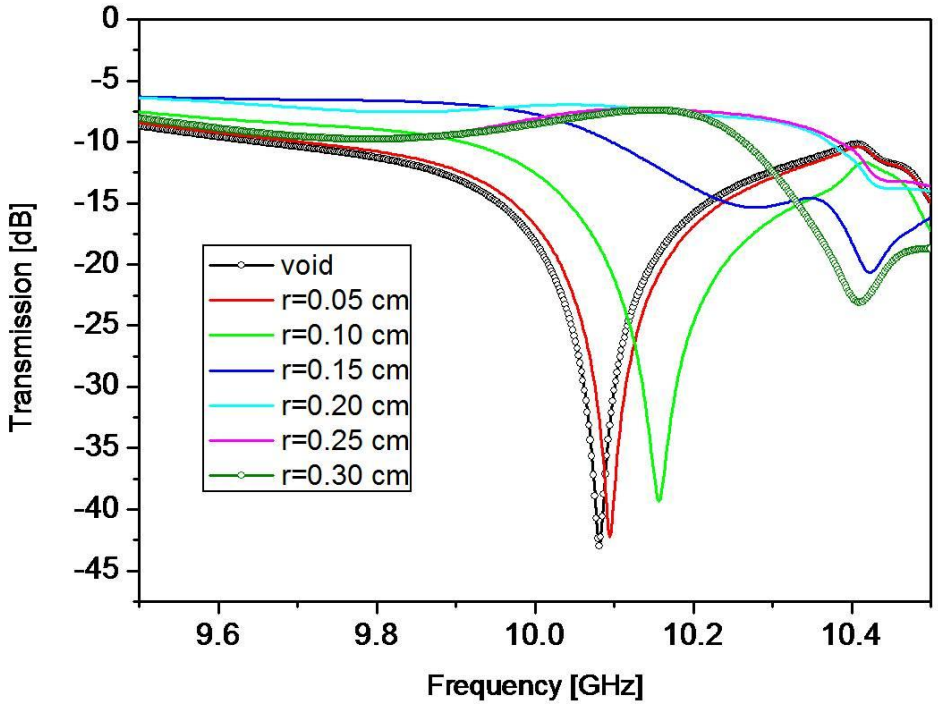


*Figure.3.20. Curves showing the dependence of the localized state on the radiusof the central pillar.*

To summarize, a photonic quasi crystal structure with very interesting transmission properties is presented. The wave guiding within the structure is affected by a defect-free localized state within the photonic band gap. As shown numerically and verified experimentally, the structure acts like a filter for the localized frequencies. The presence of the central pillar which acts like a defect alters the transmission through the waveguide. It is also very interesting to see that by changing the properties of this defect, the transmission properties of the waveguide can be tuned. Since this peculiar effects are assisted b the presence of a localized stated, they are very short range in terms of frequency. The structure therefore acts more like a photonic notch filter with a pass band of ~ 10 MHz width.

# Chapter 4

# Spatial light modulation based on Computer generated Holography for fabrication of photonic structures

Various methods are used to fabricate photonic crystals and quasicrystals. A general introduction to this topic is given in Chapter 1. This chapter is dedicated to discuss computer generated holography technique combined with the spatial light modulation to generate complex photonic structures. Before going into the details of this technique, let us have a look to some of the other holographic recording techniques, which is helpful to understand the basic idea of holographic techniques.

## 1. Multiple-beam Holography

Holography refers to the imaging technique in which the image retains the phase information about the object being imaged. This is usually done with the help of interference of coherent beams. The intensity profile produced by the interference is determined by the phase, amplitude and polarization of the interfering beams.

The electric field associated with the $m^{th}$ interfering beam can be expressed as:

$$\mathbf{E}_m = E_m exp[i\mathbf{K}_m.\mathbf{r} + i\delta_m]$$

where $E_m$ is the real amplitude, $\mathbf{r}(x,y,z)$ is the position vector, $\mathbf{K}_m$ is the propagation vector and $\delta_m$ is the absolute phase. This leads to the general expression of irradiance profile for N-beam interference as:

$$\mathbf{I}(\mathbf{r}) = \sum_{l=1}^{N}\sum_{m=1}^{N} E_l E_m \, exp\left[i(\mathbf{K}_l - \mathbf{K}_m).\mathbf{r} + i(\delta_l - \delta_{m)}\right]$$

This expression can be used to generate 2-dimensional geometries of any order of rotational symmetry.

Several holographic methods were employed to generate photonic structures. Sutherland *et al* used Switchable holographic polymer-dispersed liquid crystals (H-PDLC) materials to realize holographic gratings [45]. P.Gorkhali *et al* used H-PDLC to fabricate switchable photonic quasicrystals [28]. In this case, the quasicrystal patterns were generated by the coherent interference of multiple laser beams as described above. The pattern is recorded using a homogenous mixture of photopolymer, liquid crystals (LC) and photo-initiator. Photo polymerization occurs in the bright region of the interference pattern, which results in a counter diffusion process in which the liquid crystal diffuses into the dark regions of the interference pattern. As a result, most of the LC is captured in the low-intensity regions of the interference pattern with the polymer residing in the bright regions of the interference pattern. This leads to the photo-induced phase separation of the liquid crystal and the polymer. The separation of the liquid crystal and polymer phases depends on the intensity modulation caused by the interference pattern. Since the polymer and the liquid crystal used are usually of different indices of refraction, the intensity modulation is translated into a refractive index modulation in the recording medium because of the phase separation. Figure (4.1) shows the calculated irradiance profile of quasicrystal patterns of 5-, 7- and 9-fold rotational symmetry.

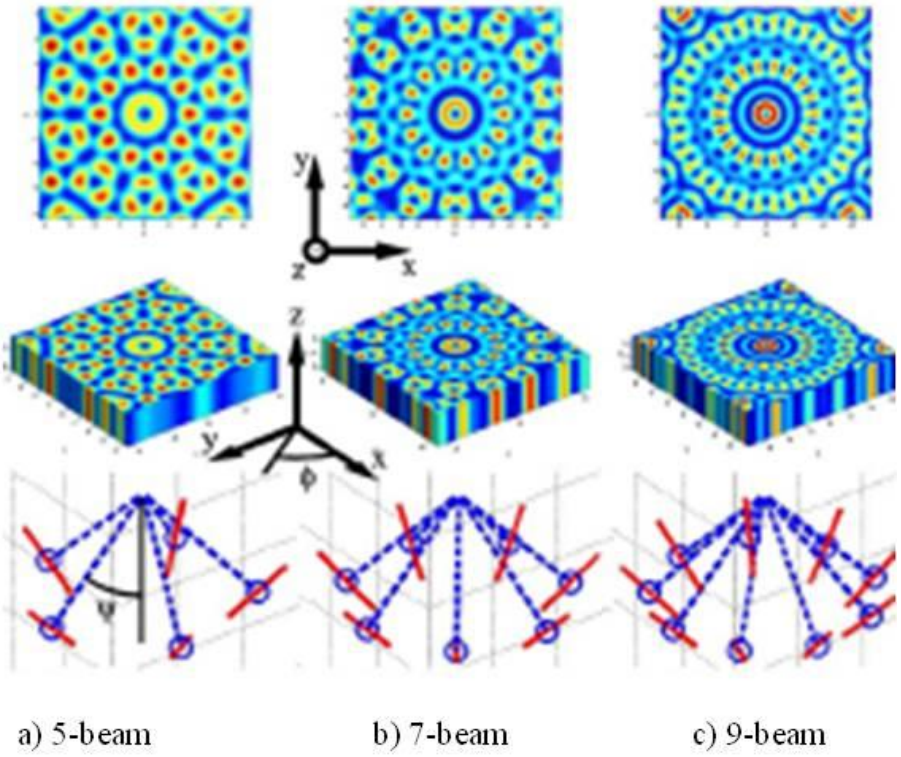


***Fig (4.1): In-plane (top) and 3-D view (middle) of the intensity profiles for 5-, 7-, and 9-fold symmetry quasi structures generated by interfering p-polarized beam.***

The resulting structure in the real space and hence the diffraction pattern are determined by the reciprocal lattice vectors. For odd $N$, there are $2N$ first-order reciprocal vectors formed considering both vectors pointing in the positive and negative directions. So the Penrose pattern, which is five-fold symmetric will have decagonal phase symmetry in the reciprocal plane. The Fourier transform of the resulting irradiance profile gives the diffraction pattern produced by the structure. The 2-dimensional discrete Fourier transform for an irradiance profile $\mathbf{I}(\mathbf{r})$ is given by the following expression.

$$F(u,v) = \frac{1}{N^2}\sum_{u=0}^{N-1}\sum_{v=0}^{N-1}\mathbf{I}(r)exp\left(-2\pi i\frac{ur\cos\theta + vr\sin\theta}{N}\right)$$

Where;

$x = r \cos\theta$ and $x = r \sin\theta$.

The diffraction peaks will have N-fold symmetry, which represent the primitive reciprocal lattice vectors. The total number of primitive reciprocal vectors is the number of ways in which $N$ points can be connected. It is also possible to predict the parameters for the interfering beams if the required diffraction pattern is already known.

The main disadvantage of this technique is that it uses multiple laser beams (equal to the order of symmetry of the crystal structure), usually obtained by dividing a single beam using beam splitters. So the experiment becomes tedious when it is needed to fabricate quasicrystals of higher order symmetry due to the difficulties in controlling the phase and coherence of a large number of beams.

Yi Yang *et al* [29] presented a single beam holographic method for the fabrication of quasicrystals. They used an optical mask to adjust the phase relation of the interfering beams. In order to get an 8-fold symmetric pattern, in the usual multiple-beam holography, one has to use 8 beams. But instead, they used a top cut octagonal prism (TCOP), which plays the role of both splitting the plane wave into eight beams and then combining the beams again to encode an intensity pattern at the bottom of the TCOP. But this method also has limitations: it needs a different phase mask depending on the symmetry of the structure. In the next section, a versatile, yet simple single beam method for the fabrication of any complex photonic structures is introduced.

## 2. Spatial light modulation by computer generated Holography (CGH-SLM technique)

The basic idea behind this technique is same as that of usual holography, to record the complete irradiance profile from an object including the phase information. But in the case of computer generated

holography, there is no need to have a real object. Instead, the irradiance profile that needs to be recorded is computed and is used to address a diffractive optical element (DOE) which spatially modulates a laser beam according to that irradiance profile. This spatially modulated beam is then used to record the pattern onto a photosensitive medium. Computer generated holography has been used for beam shaping and holographic optical tweezers to obtain the required beam profile.

In this work, a programmable spatial light modulator is used as the diffractive optical element, which encodes the irradiance profile into a liquid crystal display, the principle being the same as that used in optical trapping technology. The advantages of this method are that it allows a real-time monitoring and reconfigurability of the pattern along with a high spatial resolution. This technique can generate almost any kind of 1-or 2-dimensional patterns. The experimental set-up is much simpler than that of usual multiple beam holography. The next sections will explain in detail the various aspects of this technique.

## 2.1. Spatial Light modulator

As the name indicates, the spatial light modulator (SLM) is a device that modulates the coherent light based on its control input. The SLM uses the information about the pattern from a computer and converts the light impinging on its surface according to the pattern. The following factors characterize an SLM.

### 1. Method of addressing the SLM

The writing of the input patterns onto an SLM can be done either electronically or optically. In the electronic method, each pixel on SLM is supplied with a voltage that represents the shade and intensity of the corresponding pixel in the input pattern. This is implemented by either having an electrode for each pixel that is scanned by an electron beam

or by having addressable electrodes to which the necessary voltage is applied. In the optical method, the input pattern is converted to an optical image and is cast on the SLM.

**2. Frequency of the input beam**

The SLM will be designed to operate for a particular range of frequencies.

**3. Modulation scheme**

The SLM modulates the basic characteristics of a beam of light, i.e., amplitude, phase and polarization. The SLMs differ also in the way they modulate these properties.

Other important features of the SLMs are resolution, contrast, uniformity and number of gray levels.

The liquid crystal-spatial light modulator employed in this work is the HoloEye Photonics LC-R 3000. The system is based on a high resolution WUXGA LCoS display of 1920 × 1200 pixels with twisted-nematic cells. This SLM permits modulation of the beams in visible frequencies (600-400 nm). It can be used to modulate light spatially in amplitude and phase, where the modulation function can be addressed electrically by a computer with a frame rate of 120 Hz. The square pixel-cell size is $9.5\mu m$, whereas the filling factor of the display is 92%, on an imaged array of 19.01× 11.40 $mm$, and with a phase modulation ranging between 0 and 2π with 256 discrete levels.

The LC molecules are nematic with a twisted alignment between the parallel ITO coated plates of the cell. The electrodes driven by a computer permit to apply discrete values of voltages $V_m$ in a suitable range of 256 levels, so that m = {0,1,...,255}.The external electric field reorients the LC-molecules in each pixel-cell separately and with a fixed degree of reorientation depending of the voltage level applied. The

LC molecules are birefringent, which introduces a phase shift on the optical beam ΔΦ depending on the degree reorientation and optical path, which is

$$\Delta\Phi = \int_0^d \frac{2\pi}{\lambda}[n_e(\theta,z) - n_o]dz$$

where $n_e(\theta,z)$ is the extra-ordinary refractive index and $n_o$ is the ordinary refractive index.

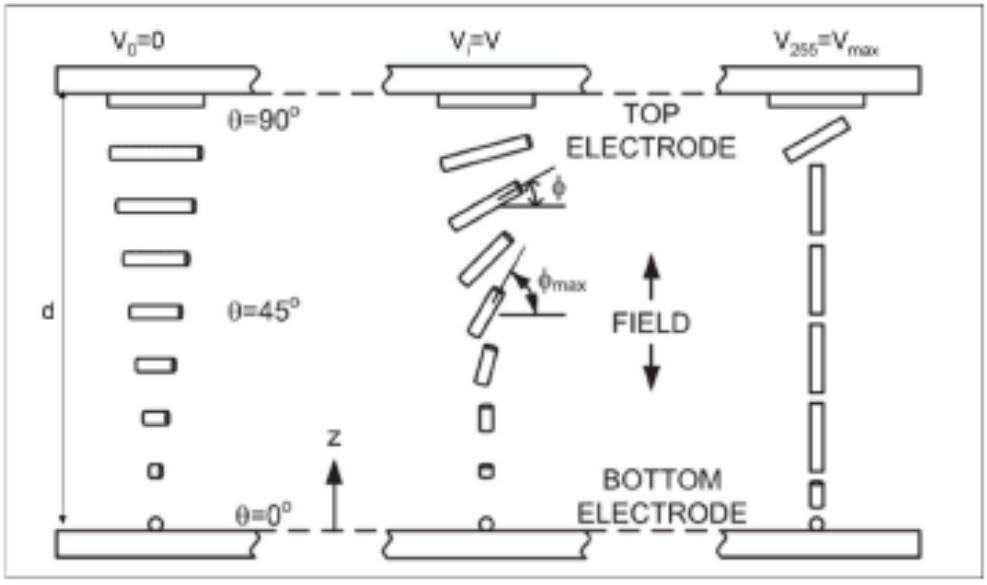


***Fig (4.2): Scheme of three nematic twisted pixel-cells in a liquid crystal spatial light modulator: a fixed voltage reorients the LC-molecules resulting in a optical phase retardation experienced by the laser beam traveling through the cell; larger is the applied voltage level, larger will be the amount of LC reorienting.***

The phase profile addressed to the SLM via the computer is thus translated to the phase retardation of the input laser beam.

The phase profiles addressed to the SLM-display are intensity images with 256 grey levels (8-bit images), each of which corresponds to a certain voltage level resulting in a phase retardation added to optical

phase of the incident beam. As mentioned before, the hologram is previously designed by computer.

## 2.2. Design of Holograms

Two different experimental approaches are used to reconstruct the photonic structure. One is based on the Fourier holographic technique and the other one is direct writing of the pattern. Depending on the method used in experiment, the design of the hologram also varies.

### 2.2.1. Principle of Fourier holography

In this technique the phase/amplitude of the hologram is designed in such a way that after diffraction, the required intensity profile is formed at the Fourier plane of the reconstructing lens. The reconstructing lens can be a simple convex lens or a microscope objective. The photosensitive recording medium will be placed exactly in the Fourier plane in order to record the required pattern.

The irradiance profile at the Fourier plane is determined by electric filed amplitude associated with the optical beam at the input plane of the reconstructing lens, $E_{in}(\mathbf{r})$, and the focal length of the lens $f$. This can be derived using the scalar Fourier transform theory as follows:

$$E_{in}(\mathbf{r}) = A_0 \exp\left[i\Phi_0 + i\Phi_{in}(\mathbf{r})\right]$$

$$E_f(\rho) = A_f(\rho) \exp i\Phi_f(\rho)$$

$$= \frac{e^{i\psi(\rho)}}{\lambda f} \int dr^2 E_{in}(\mathbf{r}) \exp\left(-i2\pi \frac{\mathbf{r}.\rho}{\lambda f}\right)$$

$$= FT\{E_{in}(\mathbf{r})\}$$

The inverse Fourier transform gives,

$$E_{in}(\mathbf{r}) = \frac{1}{\lambda f} \int d\rho^2 e^{i\psi(\rho)} E_f(\rho) \exp\left(i2\pi \frac{\mathbf{r}.\rho}{\lambda f}\right)$$

$$= FT^{-1}\{E_f(\rho)\}$$

where $A_0$ and $\Phi_0$ are the amplitude and the phase profile of the incident laser beam respectively. $\Phi_{in}(\mathbf{r})$ is the phase profile of the phase-only hologram (or CGH) added to the incident beam by means of the electrically addressed liquid crystal display. The irradiance profile at the Fourier plane is $I_f(\rho) = |E_f(\rho)|^2$ , can be designed according to the required pattern by adding the phase profile $\Phi_{in}(\mathbf{r})$ to the incident beam. Since the hologram is made of pixels, the discrete Fourier transform (DFT) can be used for the calculations which can be done using fast Fourier transform techniques.

The calculation of $\Phi_{in}(\mathbf{r})$, which is required to produce the right irradiance profile $I_f(\rho)$ is an important step in this technique. This is non-linear problem which can be solved numerically with suitable substitutions and iterations. The digital holographic profile is computed using an algorithm named Adaptive Additive algorithm (AA), in which each step of iteration needs a fast Fourier transform in two-dimension.

If we consider that the holograms consist of $N$ pixels on a regular array, according to the Whittaker-Shannon sampling theorem , the pixel size $l_f$ in the FT plane is related to the pixel size $l_{in}$ in the input plane by:

$$l_f = \frac{\lambda f}{N l_{in}}$$

The focal length $f$ of the reconstructing lens should be chosen according to the magnification requirements. Then using a system of relay lenses, it is possible to control the size of the input pixel size, $l_{in}$. This means that if we require to obtain a pattern with higher resolution than that

is permissible by the SLM configuration, these relay lenses can be of help.

It is possible, as for instance, to create phase-only holograms encoding the amplitude information of the desired beam without the need for complex holograms as demonstrated by Davis *et al* [46]. It is possible to reconstruct near-perfect holograms that permit to control both the phase and amplitude of the beam by using a SLM, as discussed in [47]. By adding several holographic focusing lenses with different focal lengths in the design of a kinoform, 3-D projections are also achievable as demonstrated theoretically by Haist [48] and experimentally by Sinclair [49].

**Experimental set-up**

A schematic diagram of the experimental set up involved in the Fourier holography is shown in Figure (4.3).The Gaussian input laser beam (at $\lambda$ = 532nm) is spatially filtered with a microscope objective-pinhole system (not shown in Fig.) and expanded before it impinges on the spatial light modulator, so to utilize entirely its modulating surface and to ensuring the best efficiency. The digital discretized CGH was computed with the AA algorithm and then addressed as intensity image with 256 levels of grey to the SLM display. The desired irradiance profile is obtained at the back focal plane of the microscope objective.

The phase only hologram, which is used to address the SLM, is transferred to the conjugate plane of the microscope objective using the relay lenses. Large focal length lenses can be used to minimize aberrations and coma. The real time monitoring of the writing process is done with the help of another microscope objective and a CCD camera. Matrix method in geometric optics can be used for the previous calculation of the experimental parameters such as various distances

involved in the experimental set-up and the required focal length of each lens involved.

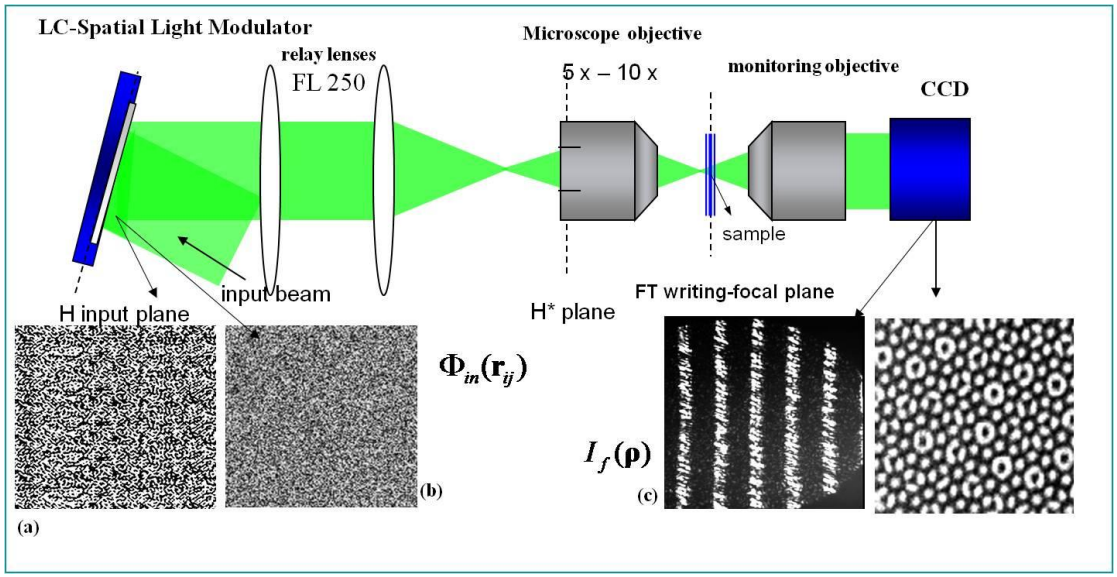


***Figure (4.3): Experimental Scheme for Fourier Holography: Figures (a) and (b) show the phase-only holograms computed to design, respectively, the irradiance profile (c) and (d): a 1-D square pattern with different sizes of dark and bright fringes (c), and a quasiperiodic octagonal irradiance profile (d).***

### 2.2.2. Direct Writing method

In this method the holograms addressed to the SLM are not the Fourier transform of the required pattern but is the pattern itself. In the direct writing method the hologram is generated in order to produce the intensity profile in the image plane of the SLM-display. This means that the writing plane in which the photosensitive sample is placed coincides with the conjugate plane of the hologram. The imaging system is realized through relay lenses as shown in the figure (4.4). As discussed by Davies *et al* [46], it is possible to encode the desired amplitude profile A(x,y) directly into a phase-only hologram Φ(x,y) with a direct method that avoids the need of the numerical iterations. The

principle is that of modulating the diffraction efficiency of the phase-only hologram along its profile by taking the product Φ(x,y)A(x,y). In this way, the amplitude profile represents the function modulating the efficiency of diffraction.

If we want to encode a function of the form

$$F(x,y) = A(x,y)\exp[i\Phi(x,y)]$$

it is needed to generate the following phase only function:

$$F(x,y) = \exp[iA(x,y)\Phi(x,y)]$$

where the new hologram is obtained by multiplying the amplitude and phase information.

A similar approach can be used in the CGH-SLM, by addressing the SLM only with the amplitude information neglecting the phase profile. Inset of the figure () shows the experimentally resulting pattern obtained for a grating.

The experimental set up in figure (4.4) uses the laser source is a Coherent doubled-frequency Verdi operating at a wavelength of λ = 532nm and impinging with an angle of < 5◦ respect to the normal to the reflective SLM-display. The desired reduced irradiance profile is reconstructed by means of two relay lenses with focal lengths ranging between 63 and 500mm depending of the wanted lateral magnification. For example if a lateral magnification of 0.1-0.2 can give a resolution of 1- 2$\mu$m since pixel size of the SLM display is 9.5 $\mu$m. The direct writing method has the same advantages of the Fourier holography scheme and solves the problem of the small cured areas of the FHS. The monitoring system is similar to the one used in the first case, consisting of a microscope objective and a CCD camera. Compared to the Fourier writing method, this technique gives a better spatial resolution.

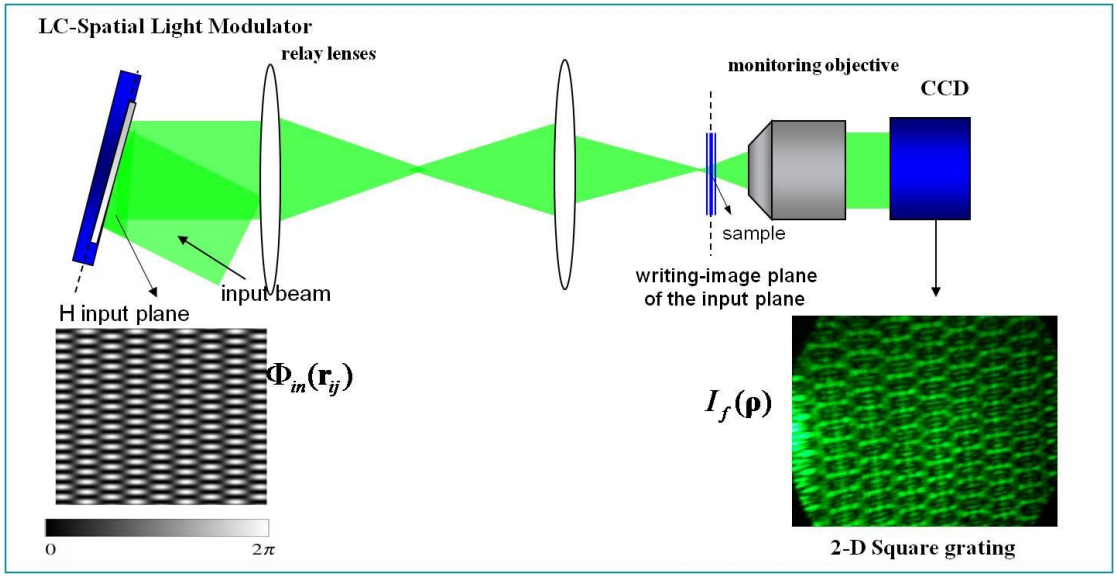


**Fig (4.4): Experimental scheme of the Direct Writing Method.**

## The photosensitive mixture and optical curing

The gratings are obtained by curing, at room temperature, a pre-polymer/LC photosensitive mixture, aiming to realize H-PDLC-like dielectric arrangements. The solution that gave the best results in terms of phase separation and optical contrast, reported in Tab.3.1, was made of the monomer dipentaerythrol-hydroxyl-penta-acrylate (DPHPA) (60.0% w/w), the cross-linking stabilizer monomer N-vinylpyrrolidinone (NVP) (9.2% w/w), the liquid crystal BL038 by Merck (30.0%w/w), and a mixture of the photoinitiator Rose Bengal (RB) (0.3% w/w) and thecoinitiator N-phenylglycine (NPG) (0.5% w/w). The approach here is similar to the H-PDLC technique described in the earlier section.

The polymer has a refractive index $n_p$ = 1.530, whereas the LC BL038 has an ordinary refractive index $n_o$ = 1.527 and an extraordinary refractive index $n_e$ = 1.799. the refractive index contrast achievable by

this mixture is $\Delta n \sim 0.2$ if the average refractive index of the liquid crystal is considered. The thickness of the sample cell varied from about 5 to 30μm, whereas the cured area has a linear dimension ranging from ~ 4 to 20mm in the Direct Writing approach, depending on the magnification factor of the imaging system. The phase separation between the liquid crystal component and the polymer depends of the typical spacing of the structure and thus the curing parameters, which are the power of the light incident on the sample and the exposure time, must be chosen in relation to the particular experimental situation. The intensity of the writing pattern was usually in the range of 1 - 20mW/cm$^2$ at the sample position, which is considering the attenuation and losses due to the optical elements, including the diffraction efficiency of the CGH addressed to the SLM. The exposure time was typically ranging between 30*s* and 300*s* depending on the writing power.

The main advantage of using liquid crystals in the recording medium is that it makes the structure switchable by applying sufficient electric field. When a sufficient electric field is applied, the liquid crystal molecules undergo reorientation, thus by changing the direction of the molecular director. This leads to the change in refractive index of the liquid crystal from ordinary to extra-ordinary. This effect can be used to generate photonic structures with switchable properties.

## 3. Experimental Results

All the patterns described below are generated by the direct writing method. The patterns are 2-dimensional quasiperiodic patterns described in the earlier chapters. The octagonal quasiperiodic structure discussed in chapter 3, is realized experimentally. The photonic band gap properties of this structure have been already discussed in section (). The samples have been realized with a tile-size around 2.5-5 μm.

The figure (4.5a) shows the theoretically calculated irradiance profile which is used to irradiate the SLM. Figure (4.5b) is the calculated diffraction pattern of the same and figure (4.5c) shows the diffraction pattern shown by the experimentally realized structure using CGH-SLM. The diffraction pattern is obtained by illuminating the structure with the radiation from a He-Ne laser at 632 nm, and it confirms the structure having the 8-fold rotational symmetry. The diffraction pattern also confirms the refractive index contrast formed between the liquid crystal and the polymer.

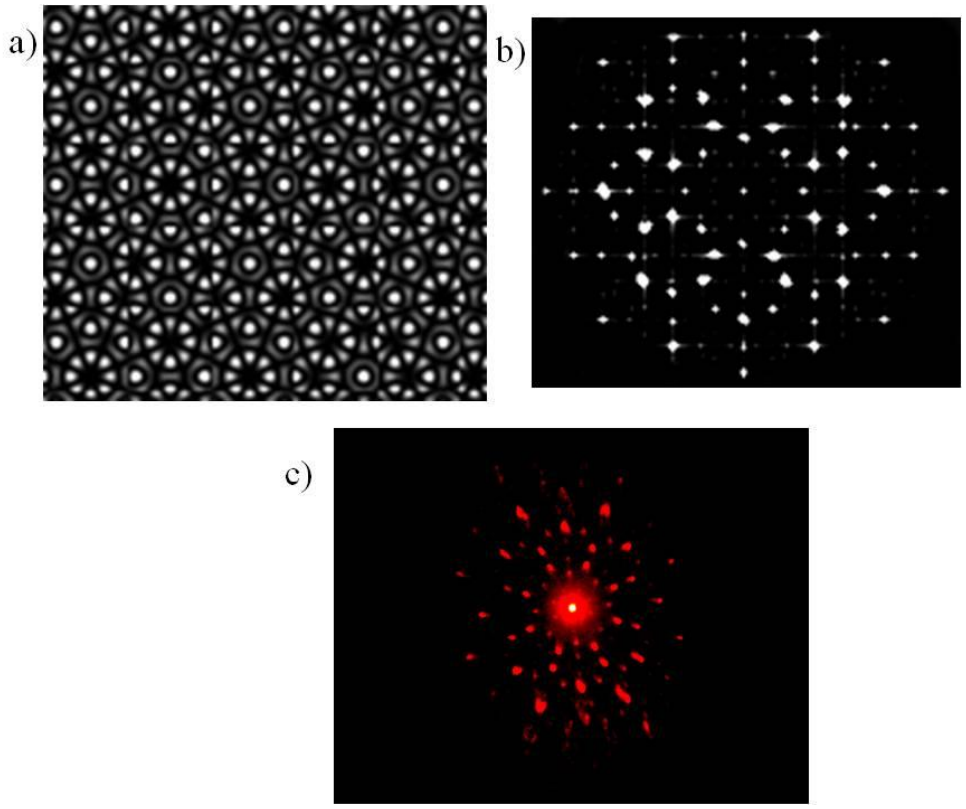


**Fig (4.5): Experimental results: (a) calculated irradiance profile, (b) calculated diffraction pattern (c) diffraction pattern of the structure obtained experimentally**

As a next step, we also tried writing patterns with some linear defect introduced. Another 8-fold symmetric pattern as shown in the figure (4.6a) is used. The writing is done in such a way that the size of the structure is big enough to be viewed through a polarized microscope. The results are shown in the figure (4.6). The aspect ratio of the structure is changed by varying the size of the pillars.

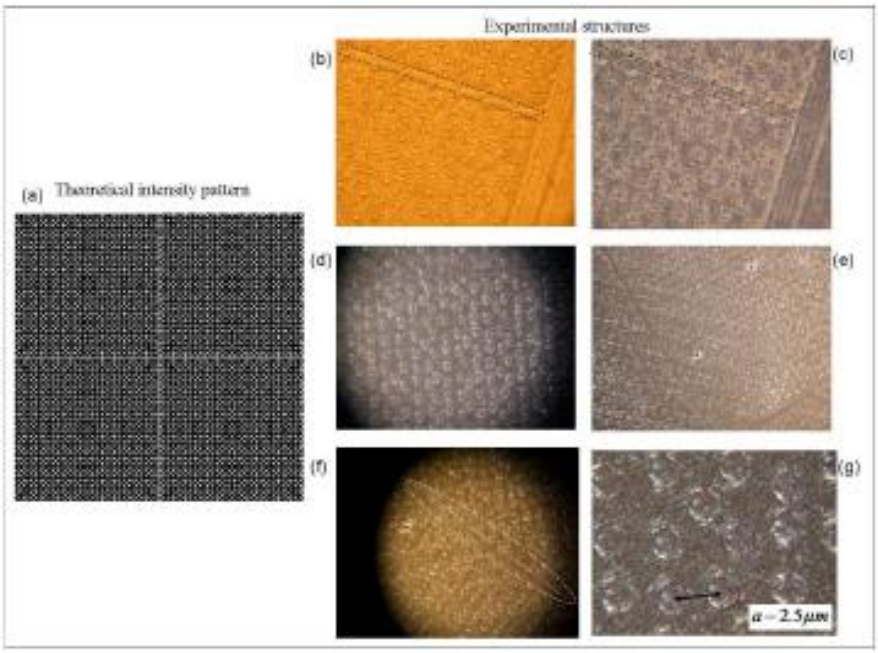


**Fig (4.6): Experimental results: 8-fold(B) quasiperiodic structures: (a) schematic representation of the intensity pattern with perpendicular defect linear channels; (b) resulting structure realized in the sample; (c) the same structure taken under crossed polarizers; (d) same quasiperiodic sample with an increased aspectratio; (e)-(f) details of the defect**

## 4. Limitations of CGH-SLM Technique

The first restriction is imposed by the minimum resolution achievable by using the SLM. The minimum resolution achievable is around 1 μm. So, when it comes to the realization of structures working in infra-red or optical frequency, the fabrication limits the frequeny of operation. The solutions to this problem are to use SLMs which offers higher

resolution or by using SLMs operated using higher frequencies. Another limitation is imposed by photosensitive mixture used for writing the patterns. The maximum refractive index attainable is very low (less than 0.2) which means it is difficult to observe any useful photonic band gap effect. One way to overcome this is to have geometries which possess band gaps with very low refractive contrasts. The studies I have done in this direction show that in most of the cases the band-gap is formed for refractive index contrasts greater than 0.3.

# Conclusions and perspectives

The research activities during this PhD were aimed for a detailed study of properties and applications of photonic quasicrystals. As a first step, the band gap formation in various photonic crystals were studied using the FDTD numerical simulations. Photonic bandgap in 2D 8-, 10- and 12-fold symmetric quasicrystalline lattices of low refractive index contrast. In particular, two different quasiperiodic spatial patterns of tiling were considered and compared for each fixed order of symmetry. It was observed that although the structures have the same symmetry, the different tiling geometry affects dramatically the existence and behaviour of the photonic bandgap. This means the rotational symmetry alone is not anough to make a prediction of the band-gap properties of quasicrystals.

To experimentally study the photonic band gap formation and the isotropy nature, an experiment is designed and conducted in the microwave regime. The experimental results matched well with the simulation results. Althoughcomplete photonic band gaps cannot exist in low-index-contrast structures, it is shown that two-dimensional band gaps are possible for specifically polarized electromagnetic modes. Notably, gaps in quasicrystal geometries are more isotropic than those in crystals, due to their disallowed rotational symmetries.

Another interesting observation is the defect-free localized state in one of the structures studied. The 8-fold interferential quasicrystal pattern showed a localized state within the band-gap frequencies. The waveguiding properties of this structure near the frequency of localization are altered by changing the properties of a central pillar placed inside the waveguide. Since this effect is very short range in terms of frequency, this effect provides a possibility of realizing optical Notch filters.

To realize the photonic quasicrystals operating in the higher frequencies, the method computer generated holography along with spatial light modulation is employed. The advantage of this CGH-SLM technique is that it is a simple, single-beam technique which allows writing of mostly any 1-, 2-or 3-dimensional patterns. Using other fabrication techniques like multiple beam holography, it is almost impossible to obtain quasicrystal patterns with higher order of rotational symmetry.

But at the moment, CGH-SLM technique is limited by the maximum refractive index contrast that can be achieved (around0.2) and the limited resolution.

Photonic quasicrystals possess interesting properties such as very high rotational symmetries. They can have photonic band gap similar to their periodic counter parts. The photonic band gaps of photonic quasicrystals can be more isotropic due to their higher rotational symmetries. Some PQC structures also show defect-free localization of electromagnetic energy due to their structural peculiarities. These properties can be very useful in making new devices. The isotropic band gaps are useful while fabricating light sources such as light emitting diodes (LEDs). Localized state assisted wave-guiding is also very useful in optical communication.

# References

[1] E. Yablonovitch, “Inhibited Spontaneous Emission in Solid state Physics and Electronics”, Phy. Rev. Lett., vol.58, p.2059, 1987.

[2] Joshua N. Winn, Yoel Fink, Shanhui Fan, and J. D. Joannopoulos, “Omnidirectional reflection from a one-dimensional photonic crystal”, Optics Letters, Vol. 23, p. 1573,1998

[3] Oncar M, Nedeljkovic D, Pearsall TP, “ Experimental and theoretical confirmation of Bloch-mode light propagation in planar photonic crystal waveguides”, Appl Phys Lett, vol. 80 , p.1689, 2002

[4] Berndt Kuhlow, Georges Przyrembel, Stephanie Schlüter, Walter Fürst, Ralf Steingrüber, and Christiane Weimann, “Photonic Crystal Microcavities in SOI Photonic Wires for WDM Filter Applications”, Journal of Lightwave Technology, Vol. 25, p. 421, 2007

[5] T. Ochiai and J. Sánchez-Dehesa, “Superprism effect in opal-based photonic crystals”, Phys. Rev. B, vol. 64, 245113, 2001

[6] D. Luo, X. W. Sun, H. T. Dai1, H. V. Demi, H. Z. Yang, and W. Ji, “Electrically tunable lasing from a dye-doped two-dimensional hexagonal photonic crystal made of holographic polymer-dispersed liquid crystals”, Appl. Phys. Lett., vol. 97, p.081101, 2010

[7] D. Shechtman , I. Blech , D. Gratias and J. W. Cahn, “Metallic Phase with Long-Range Orientational Order and No Translational Symmetry”, Phys. Rev. Lett. vol.53, p.1951, 1984

[8] G. Zito, B. Piccirillo, E. Santamato, A. Marino, V. Tkachenko and G.Abbate. Two-dimensional photonic quasicrystals by single beam computer-generated holography. Opt. Express, vol. 16, p. 5164, 2008.

[9] A-Li Chen, Yue-Sheng Wang, Ya-Fang Guo and Zheng-Dao Wang, “Band structures of Fibonacci phononic quasicrystals” , Solid State Communications, vol. 145, p. 103, 2008

[10] A.N. Poddubny and E.L. Ivchenko, “Photonic quasicrystalline and aperiodic structures”, Physica E, vol. 42, p.1871, 2010

[11] R. C. Gauthier and K. Mnaymneh, “Photonic band gap properties of 12-fold quasi-crystal determined through FDTD analysis” Opt. Express, vol. 13, p.1985, 2005.

[12] M. E. Zoorob, M. D. B. Charlton, G. J. Parker, J. J. Baumberg and M. C. Netti, "Complete photonic bandgaps in 12-fold symmetric quasicrystals", Nature, vol. 404, 740-743, 2000

[13] Khaled Mnaymneh and Robert C. Gauthier, "Mode localization and band-gap formation in defect-free photonic quasicrystals", Optics Express, Vol. 15, p. 5089, 2007

[14] R. Merlin, K. Bajema, R. Clarke, F.Y. Juang, and P. K. Bhattacharya, "Quasiperiodic GaAs-AlAs Heterostructures", Phys. Rev. Lett., vol.55, p.1768, 1985

[15] Xiujun Fu, Youyan Liu, Peiqin Zhou and Wichit Sritrakool, "Perfect self-similarity of energy spectra and gap-labeling properties in one-dimensional Fibonacci-class quasilattices", Phys. Rev. B vol.55, p.2882, 1997

[16] V. Passias, N. V. Valappil, Z. Shi, L. Deych, A. A. Lisyansky, and V. M. Menon, "Luminescence properties of a Fibonacci photonic quasicrystal", Optics Express, Vol. 17, p. 6636,2009

[17] Luigi Moretti, Ilaria Rea, Lucia Rotiroti, Ivo Rendina, Giancarlo Abbate, Antigone Marino, and Luca De Stefano, "Photonic band gaps analysis of Thue-Morse multilayers made of porous silicon", Optics Express, Vol. 14, p. 6264, 2006

[18] Y. S. Chan, C. T. Chan, and Z. Y. Liu, "Photonic Band Gaps in Two Dimensional Photonic Quasicrystals", Phys. Rev. Lett. Vol.80, p.956, 1998

[19] J. Romero-Vivas, D. Chigrin, A. Lavrinenko, and C. Sotomayor Torres, "Resonant add-drop filter based on a photonic quasicrystal", Optics Express, vol. 13, p. 826, 2005

[20] M A Kaliteevski, S Brand, R A Abram, T F Krauss, R DeLa Rue and P Millar, "Two-dimensional Penrose-tiled photonic quasicrystals: from diffraction pattern to band structure", Nanotechnology, Vol.11, p. 274, 2000

[21] A. Della Villa, S. Enoch, G. Tayeb, V. Pierro, V. Galdi, and F. Capolino, "Band Gap Formation and Multiple Scattering in Photonic Quasicrystals with a Penrose-Type Lattice", Phys. Rev. Lett., vol. 94, p.183903, 2005

[22] Y. Neve-Oz, T. Pollok, Sven Burger, Michael Golosovsky, and Dan Davidov, "Fast Light and Focusing in 2D Photonic Quasicrystals", PIERS vol.5, p.451, 2009

[23] M. Notomi, H. Suzuki, T. Tamamura, and K. Edagawa, "Lasing Action due to the Two-Dimensional Quasiperiodicity of Photonic Quasicrystals with a Penrose Lattice", Phys. Rev. Lett. vol.92, p.123906, 2004

[24] Yiquan Wang, Xiaoyong Hu, Xingsheng Xu, Bingying Cheng, and Daozhong Zhang, "Localized modes in defect-free dodecagonal quasiperiodic photonic crystals", Phys. Rev. B, vol. 68, p.165106, 2003

[25] E. Di Gennaro, D. Morello, C. Miletto, S. Savo, A. Andreone, G. Castaldi, V. Galdi and V. Pierro, “A parametric study of the lensing properties of dodecagonal photonic quasicrystals”, Photonics and Nanostructures - Fundamentals and Applications, vol. 6, p.60-68, 2008.

[26] Alessandro Micco,Vincenzo Galdi, Filippo Capolino, Alessandro Della Villa, Vincenzo Pierro, Stefan Enoch,and Gérard Tayeb, “Directive emission from defect-free dodecagonal photonic quasicrystals: A leaky wave characterization”, Phy.Rev.B., vol.79, p. 075110 , 2009

[27] Michael J. Escuti and Gregory P. Crawford, “Holographic photonic crystals”, Opt. Eng., vol. 43, p.1973, 2004

[28] Suraj P. Gorkhali, Jun Qi, and Gregory P. Crawford, “Electrically switchable mesoscale Penrose quasicrystal structure”, Appl. Phys. Lett., vol.86, p.011110,2005

[29] Yi Yang, Qiuze Li, and Guo Ping Wang, “Design and fabrication of diverse metamaterial structures by holographic lithography”, Optics Express, vol. 16, p. 11275, 2008

[30] Alexandra Ledermann, Ludovico Cademartiri, Martin Hermatschweiler, Costanza Toninelli, Geoffrey A. Ozin, Diederik S. Wiersma, Martin Wegener and Georg von Freymann, “Three-dimensional silicon inverse photonic quasicrystals for infrared wavelengths”, Nature Materials vol.5, p.942, 2006.

[31] E. Jurdik*, G. Myszkiewicz, J. Hohlfeld, A. Tsukamoto, A. J. Toonen, A. F. van Etteger, J. Gerritsen, J. Hermsen, S. Goldbach-Aschemann, W. L. Meerts, H. van Kempen, and Th. Rasing, “Quasiperiodic structures via atom-optical nanofabrication”, Phys. Rev. B, vol. 69, p.201102(R), 2004

[32] K. M. Ho, C. T. Chan and C. M. Soukoulis, “Existence of a photonic gap in periodic dielectric structures”, Phys. Rev. Lett. vol.65, p.3152(1990).

[33] J. B. Pendry, and A. Mackinnon, “Calculation of photon dispersion-relations”, Phys. Rev. Lett. vol.69, p.2772, 1992.

[34] Zhi-Yuan Li and Lan-Lan Lin, “Photonic band structures solved by a plane wave based transfer-matrix method”, Phys. Rev. E vol.67, p.046607, 2003

[35] Z.-Y. Li and K.-M. Ho, “Application of structural symmetries in the plane wave based transfer matrix method for three-dimensional photonic crystal waveguides”, Phys. Rev. B, vol.68, p.245117, 2003.

[36] X. Wang, C. Y. Ng, W. Y. Tam, C. T. Chan, and P. Sheng, “Large-area two-dimensional mesoscale quasicrystals”, Adv Mater., vol. 15 , p.1526, 2003

[37] X. Wang, J. Xu, J. C. W. Lee, Y. K. Pang, W. Y. Tam, C. T. Chan, and P. Sheng, " Realization of optical periodic quasicrystals using holographic lithography", Appl Phys Lett., vol. 88 , p.051901, 2006

[38] Y. Yang, S. Zhang, and G. P. Wang, "Fabrication of two-dimensional metallodielectric quasicrystals by single-beam holography", Appl Phyis Lett., vol. 88 , p.251104/1-3, 2006

[39] G. Zhou, and M. Gu, "Photonic band gaps and planar cavity of two-dimensional eigthfold symmetric void-channel photonic quasicrystal", Appl Phys Lett., vol. 90, p.201111, 2007.

[40] J. E. S. Socolar, "Simple octagonal and dodecagonal quasicrystals", Phys Rev B., vol. 39 , p.10519, 1989

[41] E. Di Gennaro, C.Miletto, S. Savo, A. Andreone, D. Morello, V. Galdi, G. Castaldi, V. Pierro, "Evidence of local effects in anomalous refraction and focusing properties of dodecagonal photonic quasicrystals", Phys Rev B., vol. 77 , p.193104, 2008

[42] G. Zito, B. Piccirillo, E. Santamato, A. Marino, V. Tkachenko, and G. Abbate, "FDTD analysis of photonic quasicrystals with different tiling geometries and fabrication by single-beam computer-generated holography", J Opt A: Pure Appl Opt., vol. 11, p.024007, 2009

[43] M. Bayindir, E. Cubukcu, I. Bulu, and E. Ozbay, "Photonic band-gap effect, localization, and waveguiding in the two-dimensional Penrose lattice", Phys Rev B., vol. 63, p.161104, 2001

[44] L. Levi, M. Rechtsman, B. Freedman, T. Schwartz, O. Manela, and M. Segev, "Disorder-Enhanced Transport in Photonic Quasi-Crystals: Anderson Localization and Delocalization," in Quantum Electronics and Laser Science Conference, OSA Technical Digest (CD) (Optical Society of America, 2010), paper QME2.

[45] R. L.Sutherland, L .V. Natarajan, V. P. Tondiglia andT. J. Bunning, " Bragg gratings in an acrylate polymer consisting of periodic polymer-dispersed liquid-crystal planes". Chem. Mater., vol. 5, p.1533, 1993.

[46] J. A. Davis, D. M. Cottrell, J. Campos, M. J. Yzuel and I. Moreno, "Encoding amplitude information onto phase-only filters." Appl. Opt.,vol. 38, p.5004–5013, 1999

[47] A. Jesacher, C. Maurer, A. Schwaighofer, S. Bernet and M. Ritsch-Marte., "Near-perfect hologram reconstruction with a spatial light modulator", Opt. Express, vol. 16, p.2597, 2008

[48] T. Haist, M. Schönleber and H. J. Tiziani., "Computer-generated holograms from 3D-objects written on twisted-nematic liquid crystal displays." Opt. Comm., vol. 140, p. 299, 1997.

[49] G. Sinclair, J. Leach, P. Jordan, G. Gibson, E. Yao, Z. J. Laczik,M. J. Padgett and J. Courtial., “Interactive application in holographic optical tweezers of a multi-plane Gerchberg-Saxton algorithm for three-dimensional light shaping.”, Opt. Express, vol. 12, p.1665, 2004